

© 2017 Przemyslaw Rostkowski

UNCERTAINTY QUANTIFICATION OF VISTA CHARRING ABLATOR
MATERIAL DATABASE USING BAYESIAN INFERENCE

BY

PRZEMYSŁAW ROSTKOWSKI

THESIS

Submitted in partial fulfillment of the requirements
for the degree of Master of Science in Aerospace Engineering
in the Graduate College of the
University of Illinois at Urbana-Champaign, 2017

Urbana, Illinois

Adviser:

Assistant Professor Marco Panesi

Abstract

During hypersonic trajectory through a planetary atmosphere a high heat flux environment is generated due to the friction between gas particles and the vehicle. To protect it from the excessive heat energy that is transferred to it, Thermal Protection Systems are implemented in the spacecraft's design. Current modeling tools used for the design of heat shields, however, have been shown to be unable to fully replicate material response data recorded during flight. Collaborative efforts aimed at improving current models are also difficult to establish due to restrictions placed on the access to material response data. In response, a material model free of access restrictions dubbed VISTA was devised by a research group at University of Kentucky upon which synergistic projects aimed at studying performance of charring ablators can be readily organized. In the present thesis a sensitivity study of the VISTA material model is performed with both Pearson correlation coefficients and the method of Sobol; Sobol indices are shown to be a much more robust sensitivity metric in the context of charring ablators. Uncertain parameters of the material database are then calibrated through the use of Bayesian inference rather than basic deterministic methods often used throughout scientific works. The calibrated parameters, as well as quantified uncertainty due to model structure errors and data inaccuracy, are finally propagated through onto the output where uncertainty is seen to be reduced by a large margin. An in-house developed tool named SMUQ is used to perform analyses contained in this thesis which features a PID controller modified version of the Delayed Rejection–Adaptive Method sampling algorithm.

To my parents, for their love and support.

Acknowledgments

I would first like to thank Professor Marco Panesi for giving me the opportunity to be a part of the NEQRAD research group at University of Illinois at Urbana-Champaign as well as his guidance and support of both professional and personal goals. I would also like to thank him for the chance to work on my current project concerning the calibration and validation of material models meant to predict the material response of AVCOAT; the project is funded by NASA grant no. NNX16AD18G.

I would also like to thank all members of the NEQRAD research group: Bruno Lopez, Alessandro Munafo, Andrea Alberti, Vignesh Jayaraman, Robyn Macdonald, Amal Sahai, Simone Venturi, Chiara Amato, and Maitreyee Sharma Priyadarshini.

I would like to further give my thanks to Simone Venturi who has guided me since the beginning specifically on the fundamentals of sensitivity analysis, uncertainty quantification, and coding. This is in addition to exhibiting an endless amount of patience and willingness to help at any time.

I also thank the members of the University of Kentucky research group led by Prof. Alexandre Martin whose work focuses on improving the current state of charring ablator model response tools. I would like to specifically recognize Dr. Weng as well as Ali Omidy and Justin Cooper for always being helpful with fundamentals of ablation, aspects of their KATS toolbox, and general joint project tasks.

I would like to thank my parents and my brother for the endless, unconditional support that they have given me throughout my life. I would like to extend that same gratitude to my girlfriend who is always there at my side to help me.

Finally, I would like to thank my friends back home who I've had the privilege to associate myself with since high school and new friends who I've met throughout my time on the University of Illinois at Urbana-Champaign campus.

Table of Contents

| | | |
|----------------------|--|----|
| Chapter 1 | Introduction | 1 |
| Chapter 2 | Ablation and Computational Models | 6 |
| 2.1 | Physical Behavior | 6 |
| 2.2 | Ablation Models | 8 |
| Chapter 3 | Statistical Framework | 16 |
| 3.1 | Literature Review | 16 |
| 3.2 | Sensitivity Analysis | 19 |
| 3.3 | Calibration and Uncertainty Quantification | 22 |
| Chapter 4 | SMUQ: Stochastic Modeling and Uncertainty Quantification Toolbox | 27 |
| 4.1 | Monte Carlo | 28 |
| 4.2 | Metropolis–Hastings Algorithm | 30 |
| 4.3 | Delayed Rejection–Adaptive Method MCMC | 33 |
| 4.4 | Sampling of Multimodal PDFs | 43 |
| 4.5 | High Posterior Density Regions | 43 |
| Chapter 5 | Results | 46 |
| 5.1 | Flight Scenario and Data | 46 |
| 5.2 | Sensitivity Analysis of VISTA in Apollo 4 Scenario | 48 |
| 5.3 | Calibration and Uncertainty Quantification of VISTA | 58 |
| Chapter 6 | Conclusions | 76 |
| References | | 78 |

Chapter 1

Introduction

Humanity's journey to becoming a space faring civilization began thousands of years ago when the first individual questioned the night sky and its splendidous stars and formations. Ever since that moment, the same spark of curiosity drove numerous early scientists, often at their own peril, to question the status quo and lay foundation for the scientific progress that has been achieved in the past millennia. Countless years of intellectual progress lead to the launch of Sputnik 1 on October 4, 1957, which became the first man-made object in space. Shortly after, the first human was put into Earth's orbit in 1961, and billions have gazed at the footage of Apollo program astronauts taking first steps on the lunar surface on July 20, 1969. What followed was the full realization of the potential that space exploration holds for the betterment of human lives around the globe. Now, nearly fifty years later, humanity has set its gaze upon Mars as NASA has announced plans to put astronauts on the face of the red planet in the 2030s [1]. However, as history of the space program has proven, space exploration is laden with dangers. Most recently, seven astronauts lost their lives on board space shuttle Columbia on February 1st, 2003 during the return stage of the mission. The Thermal Protection System [TPS] responsible for the protection of the vehicle from excess temperatures encountered at high velocities during atmospheric re-entry failed due to damage sustained at lift-off.

During the re-entry portion of a space mission, the vehicle plunges through the atmosphere at hypersonic speeds that exceed that of molecular motion. At these conditions, the atmospheric particles do not have enough time to move out of the way and pile up in a layer of high temperature plasma in front of the vehicle [3]. Entry vehicles are protected from the hostile conditions created during atmospheric re-entry by TPS included in their design. Charring ablaters, such as PICA and AVCOAT, are often utilized in high-speed entry missions; most notably, AVCOAT was the TPS material of choice throughout the Apollo program [4–7]. These charring ablators are manufactured by combining non-reacting, stacked



Figure 1.1: Artist rendition of capsule re-entry [2].

fiber structures with pyrolyzing phenolic resins. The end result is a material that experiences decomposition of its resin through pyrolysis at and beyond its surface during high heating conditions. Generated pyrolysis gases escape into the flow field through the porous structure while the non-pyrolyzing constituent materials are left behind in material's char state and ablate at the recessing surface [8].

The newest revision of AVCOAT has been included in the design of NASA's Multi-Purpose Crew Vehicle [MPCV] design and tested in flight on December 2014 [EFT 1] [10]. The test vehicle was outfitted with thermocouples and pressure transducers located in multiple plugs across the span of the aft heatshield which collected data throughout the entry phase. However, restrictions placed on the publication of the material properties of MPCV's AVCOAT hinder new collaborative efforts aimed at improving current modeling methods and tools. Previous works have also shown that the current design 1-D material response tools did not reliably predict heat shield performance for past missions [11–13]. In response to this, research group at University of Kentucky is in the process of developing a new, open-source AVCOAT material database dubbed VISTA (**VISTA Is Similar To AVCOAT**) [14]. The VISTA material database aims to replicate replicating the performance of AVCOAT material used during Apollo 4 and Apollo 6 test flights for which data can be found as part of open-source publication [15]. Even



Figure 1.2: Front face of the Stardust vehicle and it's charred aft heat shield [9].

though it is not the exact same material, the model allows one to assess the fundamental assumptions made concerning physical phenomena when modeling material response of charring ablators.

Availability of data collected during Apollo flights allows for calibration and uncertainty quantification schemes to be carried out on the VISTA model with the purpose of obtaining parameters that best replicate AVCOAT behavior. The simplest calibration efforts carried out in literature and industry involve manually varying select model parameters based on previous knowledge and intuition to match a set of data obtained at an experimental facility. However, with the complexity of the model and phenomena involved at hand, this approach results in calibrated models which require large safety margins to be implemented in final product designs. The parameter space of ablation models is commonly large and make manual or “one at a time” methods infeasible. Another calibration approach encountered is the inference of model parameters through the solution of the inverse problem. Usually performed from a deterministic point of view, the solution to the problem is derived by minimizing a function of error between model output and data with a regularization term [16]. The final solution is a set of parameter values that best replicates calibration data. These approaches do not account for modeling assumptions and uncertainty present in data known collectively as experimental uncertainty. Instead, in this work, the calibration of the VISTA material database is conducted through the use of Bayesian inference and

solution of statistical inverse problems [16–19]. Unlike deterministic approaches, parametric uncertainties, as well as model uncertainties due to the inadequacy of the model in representing physical phenomena and data uncertainties due to inaccuracy of measurements taken, are simultaneously quantified and expressed in the form of Probability Distribution Functions [PDF]. The methodology has been applied in the past to models used in studies of turbulent flows and non-equilibrium chemistry among others [20–27]. However, to the author’s best knowledge, this is the first time that Bayesian UQ analysis is used in the context of ablation for TPS design. Most of the literature on this subject consists of forward propagation of parametric uncertainty with little attention paid to model inadequacy [28–31]. Consequently, the results of these analyses may strongly depend on simplifying assumptions made in the physical model.

On the other hand, the Bayesian framework utilized in this thesis outlines a systematic method through which parameter, model, and experimental uncertainties are quantified and then propagated through the forward problem on the model output quantity of interest. The goal of this work is to demonstrate the use of Bayesian inference in the context of ablation, as well as to provide a calibrated version of the VISTA model database. The process conducted in this thesis is outlined as follows:

1. *Sensitivity study.* Prior to solving the statistical inverse problem, a sensitivity analysis is performed to identify most influential parameters on the experimentally observable output. Two common approaches to sensitivity analysis are carried out and the results of both are compared. Non-influential parameters are identified and excluded from calibration efforts based on the results of the approach deemed the most appropriate in the context of charring ablator problems, thereby reducing the dimensionality of the inverse problem.
2. *Calibration using manufactured data.* In the next step, data is manufactured using Apollo 4 scenario parameters and non-calibrated VISTA model parameters. The inversion process is then carried out with the use of Bayesian inference and results are compared with nominal parameter values. The purpose of this step is to demonstrate the methodology used in this work as well as to prove that information regarding uncertain parameters under consideration can be extracted from data.

3. *Calibration with experimental data.* The outlined calibration and uncertainty quantification scheme is carried out with the VISTA material database and Apollo-era aft heat shield temperature data. The calibration considers multiple sources of thermocouple data where model and experimental uncertainties are considered separately per each thermocouple location.
4. *Forward propagation of uncertainties.* Quantified uncertainties in the previous step are propagated through the statistical forward problem onto the output, and the output is then compared with data originally used in the calibration scheme.

Prior to carrying out the process outlined above, background information on the involved steps of the analysis will be given in the following chapters. Physical phenomena that occur during ablation of charring TPS materials are introduced in Chapter 2 in addition to relevant physical models. Following, Chapter 3 contains details on the theory behind sensitivity analysis and calibration through Bayesian inference utilized throughout this thesis; a short literature review is done of sensitivity studies and calibration efforts pertaining to charring ablators present in recent publications. The stated analyses shall be performed using an in-house developed code the details of which are given in Chapter 4. Finally, the results of the sensitivity study, calibration, and uncertainty quantification are given in Chapter 5 with conclusions and future work discussed in Chapter 6.

The contents of this work are part of a planned publication that will be submitted for review by the author shortly after the submission of this thesis.

Chapter 2

Ablation and Computational Models

In the present chapter, physical phenomena that occur during ablation of charring materials are discussed. The material response in this work is simulated with the Kentucky Aerothermodynamics and Thermal-response Solver [KATS] material response module [KATS-MR] which the VISTA material model is tied to. Following the discussion of physical mechanics involved in ablation, relevant models to the present study that are implemented as part of KATS-MR are reviewed. The discussions in this chapter rely heavily on the work of Weng [8] whose work should be referenced for detailed discussions concerning ablation and the computational framework of the KATS solver.

2.1 Physical Behavior

As a capsule plunges through atmosphere at hypersonic speeds, gas particles do not have enough time to move away and a strong bow shock forms in front of the vehicle. The vehicle's kinetic energy is dissipated through friction which, in turn, is then conveyed back to it through both flow-field convection as well as radiation processes that are a result of non-equilibrium chemistry in the thin shock layer. The purpose of TPS materials is to protect the substructure from the excessive heat flux. Although other types of TPS materials such as non-ablating ceramic plates and non-charring coatings exist, charring ablators are reserved for use on vehicles where high heating conditions are expected and re-usability is not a system requirement.

Charring ablators are characterized by their in-depth decomposition in addition to surface recession in high temperature scenarios. These materials are typically manufactured by first stacking layers of non-reacting fibers into a porous structure which is then filled with pyrolyzing resins that readily decompose. In the case of Apollo-era AVCOAT, a fiberglass honeycomb was first adhered to the vehicle sub-

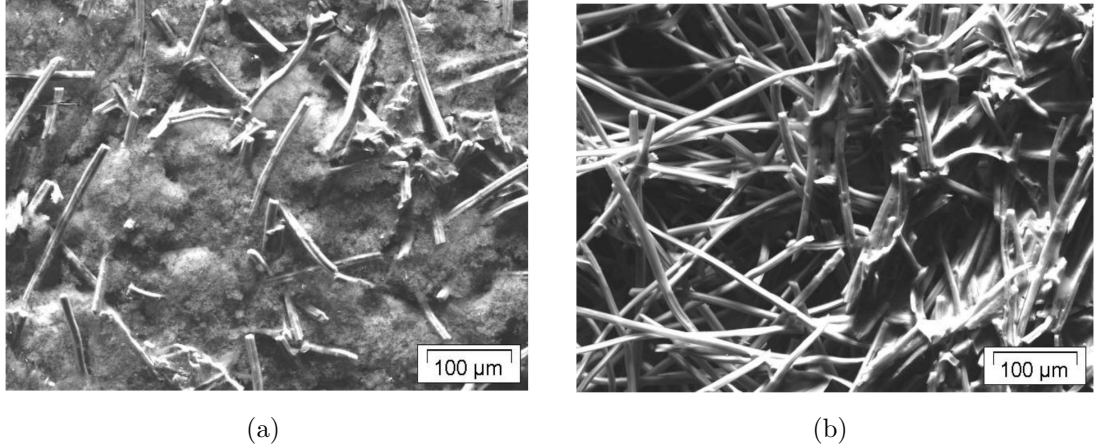


Figure 2.1: Comparison of a PICA sample in its virgin (a) and char (b) states [32].

structure; a mixture of pyrolyzing resins and silica fibers among others was then used to fill in each cell of the matrix through a manual process. The material would be shaped precisely to desired thickness at the end of the procedure [33]. The “virgi” state corresponds to the original condition of the material where no decomposition occurred. Upon being exposed to high heat flux conditions, the resin at the surface of the material and in-depth begins to decompose and generate pyrolysis gases through the process of pyrolysis; the fibers do not readily decompose and are left behind. Solid mass can be further removed through processes such as spalation, vaporization, and oxidation among others, but they are not considered in this work. A pressure differential is established as pyrolysis gases are generated which expels the gases into the flow field through the porous structure. Once the resin is completely depleted and only the fibers and any matrix material remain the material is in its “char” state. The difference between virgin and char states of a charring ablator can be seen in Figure 2.1 for a PICA sample. The char state sample is shown to be devoid of resin mass present in the virgin state of the material. The remaining fibrous structure ablates at the surface thereby showing recession in the material thickness. The material response of a charring ablator in a high heating environment is summarized in Figure 2.2.

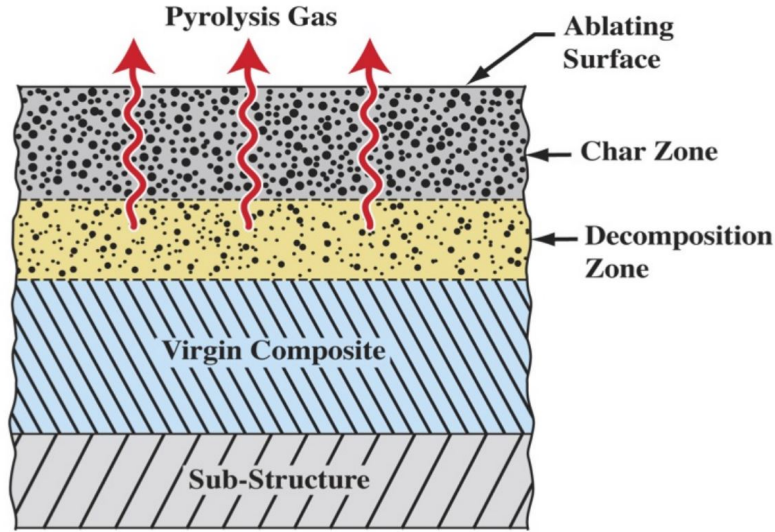


Figure 2.2: Visualization of material response of a charring ablator in high heating conditions [34].

2.2 Ablation Models

Since their inception in the early 1950s, numerous efforts have been undertaken to properly model material response of charring ablators [35]. However, the simultaneous occurrence of complex phenomena such as solid decomposition, fully dimensional heat transfer, and pyrolysis gas flows through an orthotropic porous structure among others have proven to be difficult to accurately capture with computational tools. Currently ongoing modeling efforts are taking advantage of the increased computational power available. One of these projects is the KATS solver. The material response module of KATS is designed to take into account effects of pyrolysis transport on material performance without the use of oversimplifying assumptions concerning material properties [8]. The temporal solution for the temperature of a charring ablator is obtained by numerically solving a set of governing equations: conservation equations of mass, momentum, and energy. In addition to the stated fundamental equations, in the following subsections relevant models detailing solid decomposition, porous material fluid flow, and boundary conditions are discussed. Although capable of handling 3-D problems, 1-D simulations are used to obtain model output throughout this thesis; the following equations are adjusted to reflect the use of 1-D scenarios. Ablation models and equations shown in this chapter come from Weng [8].

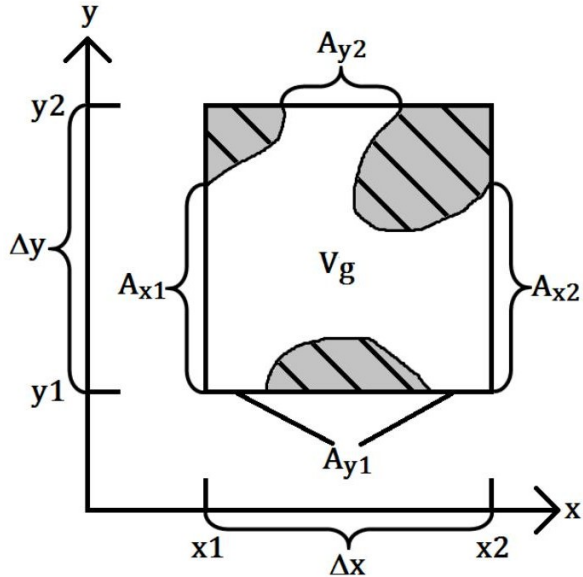


Figure 2.3: A 2-D control volume of a charring ablator [8].

2.2.1 Species Continuity

The species continuity equation enforces the condition that mass must always be conserved. In other words, the change of the amount of mass for a particular species in a control volume must be equal to the net species mass flux, in addition to the species mass generated inside the volume. A control volume for a porous, charring ablator in 2-D can be seen in Figure 2.3 where it shows the presence of both solid and gas constituents. In the case of solid species, no flow of solid mass into the control volume is possible; therefore, the change of solid species mass inside occurs solely due decomposition, as expressed by Equation 2.1. In the equation below, ρ_{s_i} is the density of an individual solid species and ω_{s_i} is the corresponding source term due to solid decomposition.

$$\frac{\partial \rho_{s_i}}{\partial t} = \omega_{s_i}, i = 1, \dots, n_{ss} \quad (2.1)$$

The pyrolysis gases are assumed to be governed by equilibrium chemistry which enables their treatment as a single species. Unlike solid material, gases are able to flow through the porous charring ablator. The volume V_g occupied by the gas in the empty voids of a porous material can be computed by taking the product of the volume of the control volume V and material porosity ϕ ; the mass of pyrolysis gases present can then be computed together with gas density. These aspects

are expressed in the gas species mass conservation Equation 2.2 where ρ_g is the density of pyrolysis gases, u is gas velocity, and ω_g is a source term due to the decomposition of solid material into gas.

$$\frac{\partial(\phi\rho_g)}{\partial t} + \frac{\partial(\phi\rho_g u)}{\partial x} = \omega_g \quad (2.2)$$

Consequently, due to the assumption of equilibrium chemistry, the source term in Equation 2.2 can be computed as follows where the volume fraction Γ is assumed to be $\Gamma_i = 1/2$ for all solid species.

$$\omega_g = - \sum_{i=1}^{n_{ss}} \Gamma_i \omega_{s_i} \quad (2.3)$$

In the case of non-equilibrium chemistry, Equation 2.2 can be readily expanded to account for multiple gas species, but the determination of individual source terms requires more complex models to be employed.

2.2.2 Momentum Conservation

The momentum conservation equation states that the net change in the momentum of gases inside of a control volume is equal to the sum of the net momentum flux through the boundaries, momentum change due to external forces applied at the boundaries, and diffusive effects of the porous material. The equation in 1-D takes the form of Equation 2.4

$$\frac{\partial(\phi\rho_g u)}{\partial t} + \frac{\partial(\phi\rho_g u^2 + p)}{\partial x} = D_x, \quad (2.4)$$

where p stands for the pressure of the gas and D_x is the diffusive effects source term. In addition to the equilibrium chemistry assumption, pyrolysis gas is also assumed to be ideal, thus allowing the ideal gas law shown in Equation 2.5 to be utilized in the calculation of gas pressure inside the material. The variables in the equation below take on commonplace definitions where R is the universal gas constant and M and T are respectively molecular weight and temperature of the pyrolysis gas. The diffusive source term is obtained with a separate model reviewed in one of the following sections that captures effects of gas flow through

porous media.

$$p = \frac{\rho_g R_u T}{M_g} \quad (2.5)$$

2.2.3 Energy Conservation

The energy conservation equation in 1-D for a charring ablator takes the form of Equation 2.6 and is based on the fact that the total energy per unit volume change of both solid and gas species is the sum of the net flux of enthalpy through the boundaries of the control volume, heat transfer due to conduction, and a diffusive effects.

$$\frac{\partial(\phi E_g + E_s)}{\partial t} + \frac{\partial(\phi \rho_g u H)}{\partial x} - \frac{\partial F_{cond_x}}{\partial x} = S_D \quad (2.6)$$

The symbols above take the following meanings: E_g and E_s are respectively total effective solid and gas energies, H is gas enthalpy, F_{cond_x} is the conductive heat flux in the 1-D case, and S_D is the diffusive source term. The conductive heat flux is computed as the product of material thermal conductivity λ and the temperature gradient. The cumulative solid species energy term E_s is obtained with Equation 2.7 where the effective density is computed by taking the ratio of the total amount of solid mass over the entire volume.

$$E_s = \rho_s c_{p,s} T \quad (2.7)$$

The diffusive source term of the energy conservation equation in a 1-D scenario is calculated with Equation 2.8 where D_x is the source term present in the 1-D momentum conservation equation.

$$S_D = D_x u \quad (2.8)$$

2.2.4 Pyrolysis Gas Transport

The high heat flux encountered during high-speed atmosphere entries causes resins of a charring ablator to decompose which, in turn, drives a build up of pyrolysis gases inside the ablator. The established pressure differential then causes the gases to be driven into the free-stream. The flow of pyrolysis gases through the porous charring ablator is modeled using a version of Darcys law [36]. The law in its basic form in 1-D is shown in Equation 2.9 where the left hand side is the

diffusive source term in Equation 2.4 and together with pyrolysis gas velocity the source term in Equation 2.6, μ is fluid viscosity, and K is the porous material permeability.

$$\nabla p = -\phi \frac{\mu}{K} u \quad (2.9)$$

The basic version of Darcy's law assumes incompressible flow and thus is unable to capture compressibility effects. The solver though is able to account for these effects through the use of a derivative of Darcy's law based on the works of Ahn et al. [37]. However, in 1-D scenarios that are the subject of this thesis, the modified expressions for the diffusive source term equate it to the expression to the right of the equal sign in Equation 2.9. Forchheimer Law alternatively is also available with the added benefit that it captures high speed flow effects through porous media [38]. In 1-D simulations the law takes the form of Equation 2.10

$$K_{xx}(D_x + b\phi^2 \rho_g u^2) = -\phi \mu v, \quad (2.10)$$

where K_{xx} is the one dimensional permeability of the ablator and b is a material specific constant, which is given for some materials by Martin and Boyd [39]. The equation above is solved for the diffusive source term D_x present in the momentum conservation and needed for the computation of the source term in the energy conservation expression.

2.2.5 Solid Decomposition Model

Upon being exposed to excessive heat flux, the resin constituent of an ablator in its virgin state begins to decompose until only the non-pyrolyzing fibers remain; the ablator is in its char state when the resin is completely depleted. A common approach to modeling solid material decomposition is through the use of a phenomenological three component approximation based on the findings of Goldstein [40]. With this model, the overall solid density is calculated with Equation 2.11

$$\rho_{st} = \Gamma(\rho_{s_A} + \rho_{s_B}) + (1 - \Gamma)\rho_{s_C}, \quad \Gamma = 1/2 \quad (2.11)$$

where $(\rho_{s_A} + \rho_{s_B})$ is the resin density, ρ_{s_C} is the density of the preform fibrous material, and Γ is the volume fraction which as stated above is assumed to take on the value of 1/2. The decomposition rate of each solid component is in turn modeled using a modified Arrhenius equation shown in Equation 2.12. The density

of each solid species decreases from its maximum virgin state value $\rho_{s_{i,v}}$ to the $\rho_{s_{i,c}}$ minimum char state value. The ψ_i parameter serves as control input over the reaction whereas A_i is the reaction pre-exponential, E_i is energy, R is the gas constant, T stands for temperature, and ω_{s_i} is the solid species decomposition rate.

$$\frac{\partial \rho_{s_i}}{\partial t} = \omega_{s_i} = -\rho_{s_{i,v}} \left(\frac{\rho_{s_{i,v}} - \rho_{s_{i,c}}}{\rho_{s_{i,v}}} \right)^{\psi_i} A_i e^{-\frac{E_i}{RT}} \quad (2.12)$$

2.2.6 Material Properties

Material properties of char and virgin states are determined apriori based on flight and ground facility data. However, the determination of material properties in the decomposition region of the charring ablator is performed through an interpolation based on char and virgin state values and degree of char parameter β . The degree of char is obtained with Equation 2.13 where it is a function of local solid density in addition to virgin and char state densities.

$$\beta = \frac{\rho_{virgin} - \rho_s}{\rho_{virgin} - \rho_{char}} \quad (2.13)$$

In turn, the β parameter can be used to compute solid and thermal material properties as shown in Equations 2.14 and 2.15 respectively. The computation of other material characteristics such as permeability and heat capacity in the decomposition layer is performed in the same manner based on the property in question.

$$\phi = (1 - \beta)\phi_{virgin} + \beta\phi_{char} \quad (2.14)$$

$$\lambda_s(T) = \frac{(1 - \beta)\rho_{virgin}}{\rho_s} \lambda_{virgin}(T) + \frac{\beta\rho_{char}}{\rho_s} \lambda_{char}(T) \quad (2.15)$$

2.2.7 Thermal Boundary Condition

A boundary condition at the front face of the domain must be specified. Similar to other works, an aerothermal boundary condition can be selected which necessitates the computation of the penetrated heat flux through the flux balance shown in Figure 2.4 on the following page [11]. In the pictured control volume affixed to the material surface, the constituent terms are: penetrated heat flux q_a , input and output radiative heat fluxes $q_{rad_{in}}$ and $q_{rad_{out}}$, conduction flux q_c ,

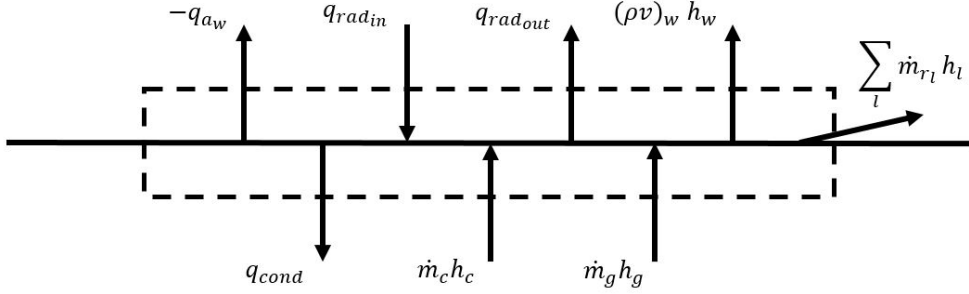


Figure 2.4: Fully expanded individual input and output heat flux balance terms for the control volume in dashes attached to the solid line surface [41].

blowing at the surface $(\rho v)_w h_w$, enthalpy fluxes $\dot{m}_g h_g$ $\dot{m}_c h_c$ and due to pyrolysis gas and char material flows rates, and the sum of energy flow due to liquidated material run-off [41]. The flux balance can be further simplified to only include the aerodynamic heatflux, radiation heat flux, and energy flux due to pyrolysis gases and material ablation terms as shown in Equation 2.16.

$$q_{pen} = q_{ah} - \epsilon \sigma (T^4 - T_\infty^4) - \dot{m}_s h_w - \dot{m}_g h_w \quad (2.16)$$

In the above equation, q_{pen} is the penetrated heat flux, q_{ah} is the aerodynamic heat flux, ϵ is material emissivity, h_w is the gas enthalpy at the wall, and \dot{m}_g and \dot{m}_s are respectively rate of pyrolysis gas blowing and rate of removal of solid material due to ablation. However, the computation of the penetrated heat flux is subject to additional uncertainties stemming from modeling errors of constituent terms such as the aerodynamic and radiative heat fluxes and gas enthalpy at the wall.

A thermocouple [TC] driver thermal boundary condition is instead selected which circumvents the need to evaluate Equation 2.16 above as well as the need to calculate the recession rate of the material. In this case, data collected from a thermocouple inside the material near the ablating surface is used as the temperature boundary condition. In reference to Figure 2.5, temperature data collected by thermocouple 1 are used as the boundary condition. The material response model then computes material temperature for locations in the material deeper than the driving thermocouple. The material sample length is consequently rescaled so that the location of the driver thermocouple is at the origin of the domain. As

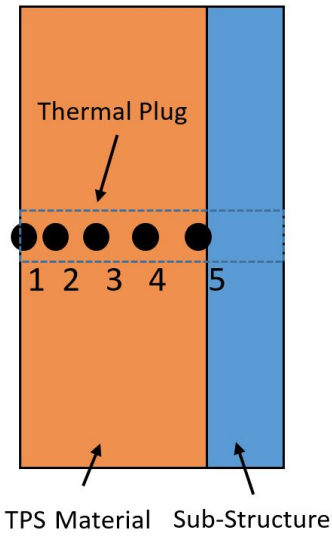


Figure 2.5: Simplified view of a thermal plug and thermocouple set up in a vehicle's heat shield.

a result with the TC driver approach, the surface boundary heating problem is decoupled from the material heat transfer study inside the ablator [29].

Chapter 3

Statistical Framework

In this chapter, a literature review of recently undertaken efforts in calibration and uncertainty quantification of models that aim to predict material response performance of charring ablators is first performed. Following, a brief introduction to sensitivity analysis is given with particular attention being drawn to two common methods often invoked throughout scientific publications, Pearson correlation coefficients and the method of Sobol. An overview is subsequently given of the basic fundamentals and theory involved in performing model calibration and uncertainty quantification through Bayesian inference. This chapter concludes with a general road map which can be utilized in calibration and validation efforts of computational models when experimental data is available.

3.1 Literature Review

In the context of charring ablators, scientific publications on the calibration and uncertainty quantification of relevant material response models is scarce. Recently the following works on the calibration of models dealing with ablating materials (charring and non-charring) and corresponding material properties have been published to the best of author's knowledge:

- Using the Charring Material Ablation [CMA] code, Molavi et al. [42] performed sensitivity analysis and model parameter inversion in order to demonstrate their approach to parameter estimation from data. The subject test case consisted of a fictitious scenario with a small sample of non-pyrolyzing ablating material. Model parameters that are a function of temperature, such as heat capacity and thermal conductivity, did not have a prescribed form, and instead, individual values at regular temperature intervals were considered. Sensitivity analysis in this work consisted of computing sensitivity indices, which were based on the computation of first order derivatives

of the output quantity of interest with respect to individual parameters. The inverse methodology performed was based on the Levenberg–Marquardt method where iterative sampling of the model parameter space was done in order to minimize a function of the squared error between model output and data. The method was proven to be able to retrieve known material parameter values from simulated data.

- In the paper by Copeland et al. [31], material property PDFs were constructed using statistical measures for the PICA charring ablator used in the Mars Science Laboratory [MSL] spacecraft design. An uncertainty quantification study was carried out by forward propagating parameter PDFs through the FIAT solver. It was found that material properties showed mutual dependence and consideration of relationships between parameters is necessary in similar future efforts. Following, a gradient oriented sensitivity analysis was performed by slightly perturbing nominal property values in order to study dominant physical phenomena. A study of parameter uncertainty contribution was also done through both the computation Pearson correlation coefficients and the method of Sobol. Differences between final results of both methods were observed suggesting that higher-order effects are influential and linear based sensitivity methods may be, therefore, insufficient.
- Mahzari et al. [29] performed uncertainty quantification, sensitivity analysis, and inverse estimation of select properties for the MSL heating environment as well as the model temperature output of the TPS material. The utilized approach in the paper implemented the TC Driver boundary condition using temperature data recorded during the entry phase into Mars’ atmosphere. The first step of the analysis consisted of applying numerical treatments to the inverse estimation of heating rates. Next, probability distributions corresponding to material parameters were forward propagated through the problem to quantify uncertainty present in the temperature output due to parameter uncertainty; a regression analysis was performed to identify contributions to the total uncertainty due to each parameter. It was found that the thermal conductivities of the charring ablator’s virgin and char states were by far the largest contributors of uncertainty. The authors went on to state that it is not possible to calibrate specific heats and thermal conductivities simultaneously in the presence of measurement errors due to

their mutual correlation. The inverse methodology outlined by Mahzari in Ref. [30], which depends on the minimization of a function based on the squared error between model output and flight error, was applied in tandem with FIAT and MSL flight data. The calibrated results consisted of decreased thermal conductivity values accompanied by a decrease in error between model output and data.

- In the work of Turchi et al. [28], two different uncertainty quantification approaches were applied to thermo-chemical ablation models. The investigated test case consisted of a sphere made of non-pyrolyzing carbon material in a scenario similar to that encountered in plasma wind tunnel ground facilities. Uncertainty quantification methodologies that were employed consisted of an anchored-ANOVA approach as well as a polynomial chaos surrogate model based on Wiener-Askey scheme. These two techniques were used to propagate parameter uncertainties through the forward problem onto model outputs. It was found that both approaches, when applied to the relevant models, yielded approximately same results.

A common theme across selected works, and others not explicitly mentioned here due to repetition of same methodology, is that uncertainty quantification of model performance is carried out by forward propagating model parameter distributions that are constructed based on current knowledge held by the investigators. The inability of models to perfectly replicate effects of physical phenomena is either not accounted for in the forward propagation or is assumed to be a certain magnitude based on the current state of knowledge. In addition, across works concerning calibration of computational models, employed inverse methodologies are typically based on deterministic methods that seek to minimize some function of the difference between model output and calibration data with little consideration to structural model and data error. Sensitivity studies are also often based on linear measures that can lead to misleading conclusions, as pointed out in one of the reviewed works. The analyses can, therefore, be improved by forward propagating parameter distributions that do not solely depend on knowledge of the investigators and take into account model inadequacy and data uncertainty.

3.2 Sensitivity Analysis

Models can be thought of as processors that relate output to the values of model and scenario parameters in an effort to replicate some real-life phenomena. Scenario parameters are, however, most often known apriori before executing the model, thus the remaining degrees of freedom are associated with model parameters. Relationships between model parameters and output also vary based on the complexity of the physical phenomena that is being captured. In the simplest of cases, the relationship between the two is purely linear with incremental increases in the value of any model parameter corresponding to proportionate changes in the values of predicted quantities of interest. These cases are, however, rare and non-linear relationships between individual parameters as well as combinations of parameters and output are more often observed. Each parameter can have a varying effect over model output where, while some parameters can have an overwhelming influence over model predictions, others may be negligible. If a model output displays low sensitivity with respect to a particular parameter, then calibration with data corresponding to that same output will yield little gain on the knowledge of that parameter; large amount of knowledge is expected to be acquired if opposite is true.

In order to study output sensitivities prior to performing model calibration, a sensitivity study is done by varying the model parameters using a Monte Carlo sampling algorithm. Sensitivity analysis at its core is a study of the relationship between model output and model parameters. As stated in Saltelli et al. it is, “the study of how the variation in the output of a model (numerical or otherwise) can be apportioned, qualitative or quantitatively, to different source of variation and of how the given model depends upon the information fed into it” [43]. The analysis is meant to give insight into the importance of each parameter which then makes it possible to rank the parameters based on their contributions to the output variation. Furthermore, it is then possible then to exclude the non-influential parameters from further analysis thereby reducing the dimensionality of the inverse problem and associated computational costs. Numerous approaches towards sensitivity study have been devised and can span from low cost screening methods and scatter plots to global variance based formulations that sample the high dimensional model parameter space [43–46]. These methods vary based on corresponding number of required model runs as well as their ability to capture non-linear relationships aspects between model parameter space and output. A

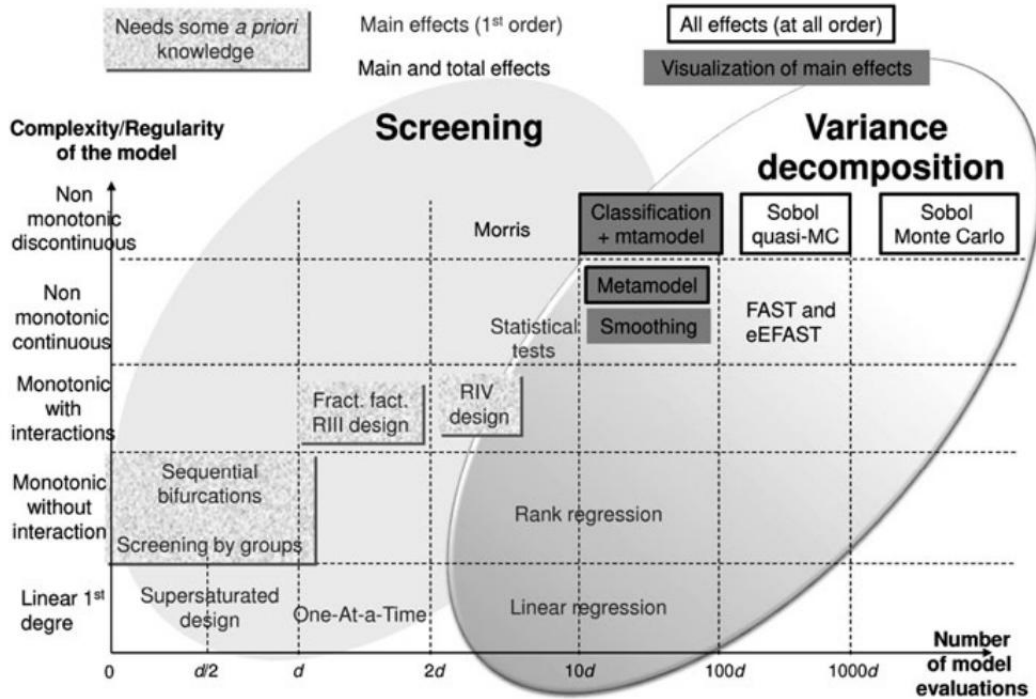


Figure 3.1: Review of sensitivity analysis methods used in literature based on their computational costs and ability to capture different input/output relationship types [46].

quick overview of sensitivity analysis techniques is given in Figure 3.1.

In this work, two commonly used sensitivity analysis measures, Pearson Correlation Coefficients [PCCs] and Sobol indices, will be compared and the applicability of each with respect to ablation problems will be evaluated. The results of the most appropriate method will be used to rank the parameters based on influence for the Apollo 4 scenario. The temperature of the charring ablator material will be the quantity of interest during the sensitivity study.

3.2.1 PCC vs. Sobol Indices

Computation of PCCs is one of the most commonly used sensitivity analysis methods in sciences due to the ease of its implementation and understanding. These sensitivity measures indicate the degree to which two variables are linearly correlated with each other and can take on values from -1 to 1 respectively indicating a very strong negative or positive relationship; a value near zero denotes

no correlation. Sample PCCs between two variables are computed with Equation 3.1 [43] which states that it is the ratio of the sample covariance between two variables and square root of the product of sample variances of each.

$$r_{x,y} = \frac{\sum_{i=1}^N (x_i - \bar{x})(y_i - \bar{y})}{[\sum_{i=1}^N (x_i - \bar{x})^2]^{1/2} [\sum_{i=1}^N (y_i - \bar{y})^2]^{1/2}} \quad (3.1)$$

The x_i and y_i quantities in the equation above represent individual parameter and output samples, barred quantities are respective sample means, and N represents the total number of samples obtained.

However, charring ablator scenarios involve numerous interacting physical phenomena that, in turn, introduce non-linearities to the system. Where relationship between model parameters and output may not be linear or monotonic, PCCs, which are a linear measure, are not robust importance indicators and may lead to incorrect conclusions. Researchers aware of non-additive aspects of their models instead turn to approaches that can capture non-linear relationships between input and output in their sensitivity studies. One of these approaches is the method of Sobol, based on the work of the Russian mathematician Ilya Sobol, and is carried out through the calculation of Sobol indices. The derivation of these indices is based on the decomposition of output variance V into separate sums of variances due to input parameters and their interactions as shown in Equation 3.2 [47].

$$V = \sum_{j=1}^k V_j + \sum_{i < j} V_{ij} + \sum_{i < j < l} V_{ijl} + \dots + V_{1\dots k} \quad (3.2)$$

This decomposition of variance based method holds no assumptions on the relationship between input and output (linear, monotonic, non-linear, ...) and allows for the consideration of interaction effects between parameters on model output. The indices are obtained through following computations:

$$S_i = \frac{V_i}{V} \quad (3.3)$$

$$S_{i_1, \dots, i_s} = \frac{V_{i_1 \dots i_s}}{V} \quad (3.4)$$

where Equation 3.3 is for first order Sobol index that captures the influence of a parameter on the output due to main effects. Higher order indices computed using Equation 3.4 capture non-primary effects between a parameter and others

with increasing dimensionality. A summand of primary and higher order Sobol indices yields the total effect Sobol index as shown in Equation 3.5 which is the focus of the sensitivity study performed in this thesis. While individual total order Sobol indices can vary from 0 to 1, the sum of these indices over all parameters can range from 1, if the model is purely additive, to more than 1 if interactions between parameters are present. This property consequently enables the inference of the degree of non-linearity present in the model input and output relationship based on the magnitude by which the sum exceeds the value of 1.

$$S_{T_i} = S_i + S_{ij, i \neq j} + \cdots + S_{1\dots i\dots s} \quad (3.5)$$

Whereas PCCs denote the degree of correlation between two variables, results of the computation of total order Sobol indices can be understood as the portion of the output variance that can be explained by the variation of a particular parameter. However, the ability to capture non-linear effects on the output comes at the expense of a much larger number of model runs required for accurate results than for the computation of PCCs as can be seen in Figure 3.1.

3.3 Calibration and Uncertainty Quantification

In all but simplest of cases, models that aim to replicate physical phenomena take advantage of simplifying assumptions. Although making the system under study less difficult to handle and computationally cheaper to execute, the approach results in uncertainty in model output. Deterministic calibration methods that aim to solve the inverse problem of obtaining parameter values from data by minimizing a weighted function of error between output and experimental data do not provide the means alone to consider uncertainty due to model inadequacy; these approaches also do not take into account uncertainty present in recorded data. On the other hand, calibration through Bayesian inference enables characterization of uncertainties associated with parameters, modeling, and data [16]. The systematic characterization of uncertainties enables a rigorous application of uncertainty quantification to be applied that does not involve propagating through the forward problem assumed model inaccuracies and prescribed parametric uncertainty. In the following subsections, the framework for calibration and uncertainty quantification through a Bayesian approach is outlined.

3.3.1 Fundamental Theory

The calibration procedure in this thesis rests fundamentally on the use of Bayes' theorem. The theorem itself stems from the elementary product rule of probability theory which states that given events A and B the probability of both events occurring can be computed with Equation 3.6. In other words, the joint probability of both events is the product of the conditional probability of event B given that event A is true multiplied and the probability of event A . Similarly, the same formula can be applied in reverse to the joint probability of both B and A occurring as expressed through Equation 3.7.

$$P(A \cap B) = P(B|A)P(A) \quad (3.6)$$

$$P(B \cap A) = P(A|B)P(B) \quad (3.7)$$

The two joint probabilities are symmetric and equivalent. Equating both Equation 3.6 and Equation 3.7 to each other gives rise to Bayes' theorem:

$$P(B|A) = \frac{P(A|B)P(B)}{P(A)}. \quad (3.8)$$

It is important to note that, while it is not included in the equations above to avoid unnecessary clutter, all constituent probabilities are in addition conditional on information that is currently known [17].

The interpretation of Equation 3.8 is subject to whether a Bayesian interpretation or a frequentist approach is taken. From a frequentist point of view, probability is a measure of the “frequency in an ensemble” [48]. Within this framework, Bayes' theorem expresses the portion of outcomes with the result B out of the outcomes A as a function of the proportion of outcomes with the result of A out of outcomes B in addition to terms describing the proportions of outcomes with results of A or B in the ensemble. On the other hand, the Bayesian framework relies on an interpretation of probability as a measure of “reasonable expectation” based on current knowledge if only a single outcome was collected [48]. With the Bayesian interpretation, Bayes' theorem expresses the updated state of knowledge of B based on evidence A as a function of the prior separate beliefs in A and B as well as the likelihood of A based on the state of knowledge of B . A further extension to Bayes' theorem in the Bayesian framework was made by Sivia and Skilling where they replaced the events A and B with *hypothesis* and *data*. In

doing so, Bayes' theorem was reinterpreted as the relationship shown in Equation 3.9; this time the dependence on background information I has been included [17].

$$P(\text{hypothesis}|\text{data}, I) \propto P(\text{data}|\text{hypothesis}, I) P(\text{hypothesis}|I). \quad (3.9)$$

In the above formulation, the probability of data was omitted due to the term serving as a normalization constant. The term is ignored in most implementations of Bayesian inference methodology as will be discussed in Chapter 4.

The extension given above can again be rewritten to more appropriately fit the calibration problem at hand. Respective to the current context, the hypothesis consists of a set of parameters $\boldsymbol{\theta}$, that combined with the model at hand, is thought to result in model output \mathbf{y} which would be identical to data \mathbf{D} ; all background information is contained within model M under study. With these definitions, the probability of the above statement being true based on supplied data, known as the posterior, is given by Equation 3.9 which is a rewritten version of Equation 3.10 where $L(\mathbf{y} = \mathbf{D}|\boldsymbol{\theta}, M)$ is referred to as the likelihood function while $P(\boldsymbol{\theta}|\mathbf{D}, M)$ and $P(\boldsymbol{\theta})$ are respectively posterior and prior distributions.

$$P(\boldsymbol{\theta}|\mathbf{D}, M) \propto L(\mathbf{y} = \mathbf{D}|\boldsymbol{\theta}, M) P(\boldsymbol{\theta}|M) \quad (3.10)$$

The prior distribution represents the probability of the hypothesis being true based on the current state of knowledge that the investigator might have obtained through literature reviews, past experience, etc. Provided that prior knowledge with respect to each θ_i is independent of others, the expression for the prior distribution takes the form of Equation 3.11 where it is a product of individual parameter prior distributions. It is important to bring attention to the fact that if stochastic models are present in the model, and corresponding hyper-parameters are part of the hypothesis statement, an adjustment to the prior distribution formulation below will have to be made to account for the presence of a second hierarchical level.

$$P(\boldsymbol{\theta}|M) = \prod_{i=1}^{\# \text{ of } \theta_i} P(\theta_i|M) \quad (3.11)$$

Individual prior parameter distributions can take on any form that accurately represents the current state of knowledge. These formulations can vary from the least informative uniform distributions where only minimum and maximum range limits are known to more specific Gauss distributions.

The likelihood function, on the other hand, describes the modeling error. It gives the probability of obtaining data \mathbf{D} based on the choice of model M and parameters $\boldsymbol{\theta}$ in the hypothesis in addition to uncertainty introduced by model inadequacies. The form of the likelihood function depends on the chosen error structure of model and data. The choice of different likelihood formulations was investigated by Miki et al. when applied to non-equilibrium chemistry models and serves as a good example of the possible variability of likelihood function forms due to factors such as additive or multiplicative data error assumptions, statistical dependence between data points, etc. However, all investigated formulations included a parameter that expressed the uncertainty in the model output caused by model inadequacy and error in recorded data. The inclusion of this parameter in the hypothesis in Equation 3.10 allows for a rigorous quantification of uncertainty due to these sources; this feature mitigates the reliance on prior assumptions concerning model and data accuracy.

The solution to the calibration problem with Equation 3.10 is obtained by updating prior state of knowledge with the likelihood function, in tandem with data obtained for observable quantities, into the posterior distribution. The process of updating knowledge through Bayes' theorem with newly acquired data is known as Bayesian inference. Fundamental to this approach, the state of knowledge to be updated is expressed in the form of PDFs which consequently forces the updated state of knowledge on parameter values to be expressed in a probabilistic manner. The inverse problem to be solved is therefore reformulated as a statistical inverse problem due to the treatment of parameter knowledge as PDFs which express corresponding uncertainties in parameter values. In turn, the propagation of updated state of knowledge in probabilistic form through the forward problem reformulates it as a statistical forward problem where the calibrated model output for the quantity of interest is also a PDF. Uncertainty quantification is performed through simultaneous forward propagation of uncertainty associated with each parameter as well as quantified model inadequacy and data uncertainty onto the output. The overall process does not specify the form of the model in study, and instead is treated as a variable which makes the approach applicable in a wide variety of fields where a relationship between input and output is present. The quantity of interest in this thesis coincides with available data hence the basic approach outlined in this chapter is sufficient. However, when calibrating models with data that do not consist of the quantity of interest, appropriate methodology extensions must be made. The necessary modifications can be found in Ref. [49]

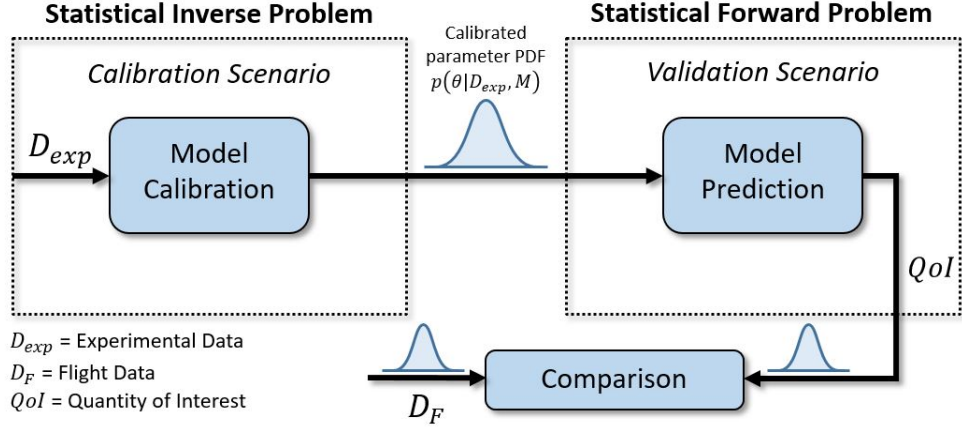


Figure 3.2: Roadmap to calibration, uncertainty quantification, and validation using Bayesian inference [20].

which utilizes Bayesian inference in combination with embedded stochastic models at the source of model error.

3.3.2 Calibration and Validation Road Map

The approach outlined in this thesis is summarized in Figure 3.2 and can be applied in general with other computational models. First, the statistical inverse problem is solved to obtain calibrated model parameters. The solution process consists of updating prior information into posterior parameter PDFs using newly acquired data; calibrated parameter PDFs express updated knowledge with respect to their values. Next the uncertainties associated with each parameter as well as the parameter that indicates the uncertainty due to modeling and data collection errors are propagated onto the quantity of interest. Results of the statistical forward problem are then compared with data in the final step. In a typical validation scenario, the forward problem would be solved using a new set of scenario parameters and results compared with data corresponding to the new scenario. However, as will be justified in following chapters, experiment and flight data in this work are chosen to be equivalent; the forward problem scenario is identical to the one used in the solution of the inverse problem.

Chapter 4

SMUQ: Stochastic Modeling and Uncertainty Quantification Toolbox

Methodology outlined in Chapter 3 forms the foundation of the in-house developed Stochastic Modeling and Uncertainty Quantification [SMUQ] toolbox written in Fortran. The computational framework of SMUQ has already in most part been covered in Ref. [49] but the summary of implemented algorithms in addition to recent improvements made to the toolbox’s solution methodology is done here for convenience. It is worth noting that software packages implementing uncertainty quantification and calibration approaches already exist such as the following: DAKOTA by Sandia National Laboratories [50], UQTools by NASA [51], and QUESO by University of Texas at Austin [52]. However, any analysis would be constrained by the methodologies utilized in existing code. Implementation of new methods would either be difficult to achieve given the complexity of existing software, which may consists of algorithms meant for non-UQ purposes, or not possible due to user end agreement conditions prohibiting tampering with software framework. The SMUQ toolbox was therefore devised as both an educational tool as well as a platform on which new methodologies can be implemented. The toolbox was also designed in a way which makes it possible to easily perform analysis outlined in Chapter 3 with any given model without the need to alter the main code of either the computational model being investigated or SMUQ.

The calibration of a computational model through Bayesian inference requires the posterior solution PDF of Equation 3.10. However, an analytical solution is not feasible in all but the simplest cases where the number of dimensions (number of uncertain parameters) is small. Simple statistical measures of distribution characteristics typically employed such as mean, median, and variance do not provide large utility when distributions under consideration show multi-modal behavior. A different approach must be instead taken which involves sampling of the posterior distribution. As stated by Tarantola, “To sample a probability density means to generate (independent) points that are samples of it, i. e. such that the probability of any of the points being inside any domain \mathcal{A} equals the

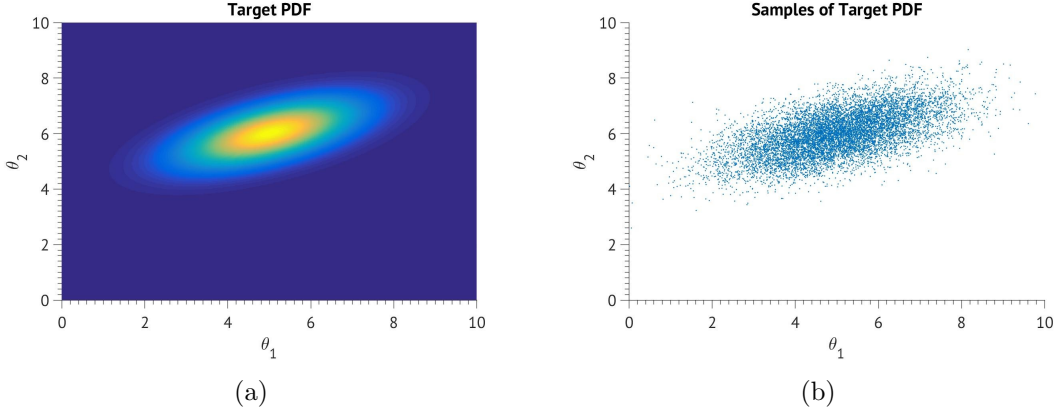


Figure 4.1: An example of a target 2D PDF (a) and its sampled counterpart (b).

probability of the domain \mathcal{A} ” [16]. The methodology implemented in SMUQ that is used to sample the posterior distribution solution and produce marginalized posterior PDFs for each parameter is described in the following sections in this chapter. A means of evaluating quality of results that the outlined calibration process yields is also presented.

4.1 Monte Carlo

The broad category of algorithms where high-dimensional spaces are explored through random sampling are called the Monte Carlo [MC] methods. These methods are widely used in problems where the solution complexity is too great for the derivation of an analytical result. Monte Carlo methods in general are used where problems associated with distribution sampling, estimation of quantities such as high-dimensional integrals, and optimization are encountered [53]. An example of distribution sampling with a basic MC method defined by a two-dimensional input domain is shown in Figure 4.1.

The purpose of an MC algorithm when sampling a probability distribution is to explore regions of significant probability. However, when exploring high dimensional probability spaces regions of significant probability can be extremely small compared to the entire high-dimensional domain. This idea can be demonstrated by drawing a unit square with a circle of unit diameter inscribed within it as shown in Figure 4.2. If a uniform distribution is assumed where every point has an equal probability of being sampled, the probability of a drawn point being inside of the circle is the ratio of the area of the circle to the area of the square

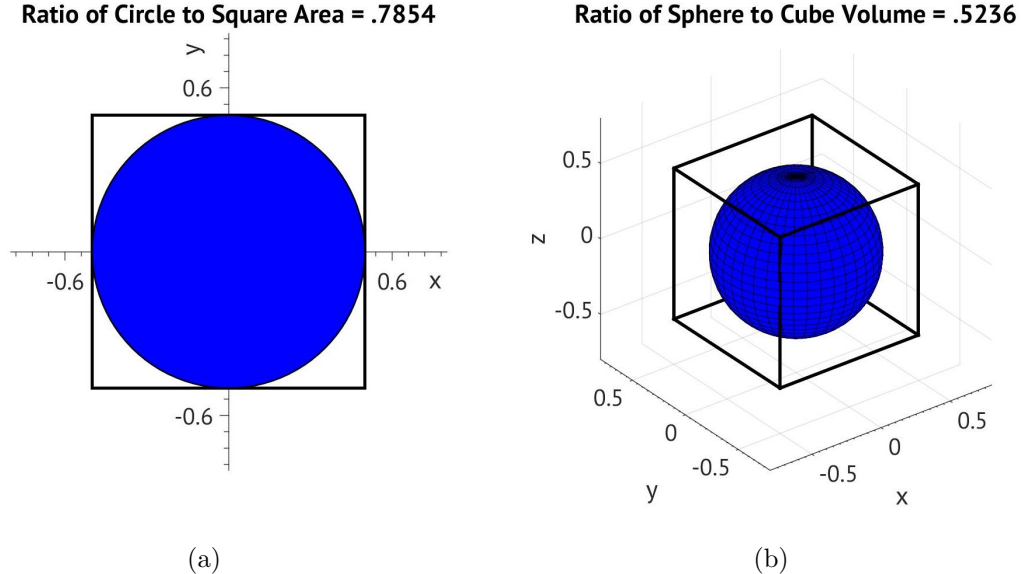


Figure 4.2: Visualization of the ratio of hypersphere and hypercube volumes in 2-D (a) and 3-D (b).

which is approximately equal to 0.7854, while in 3D this probability is 0.5236 and corresponds to the ratio of the volumes of a unit sphere and cube. With increasing dimensionality of the domain the probability of drawing a sample located inside of a hypersphere which is inscribed inside of a unit hypercube declines quickly and the “curse of dimensionality” becomes more evident with MC approaches. This quick decline in probability up to 11 dimensions is shown in Figure 4.3 where the probability of drawing a sample inside of a 11-D unit hypersphere inscribed within a unit hypercube is nearly zero. The empty space in terms of PDF sampling schemes corresponds to extremely low probability regions, consequently extensive sampling of these regions is a waste of computational resources.

Based on this information the sampling of probability distributions can be improved upon by first identifying regions of high probability and then sampling those regions efficiently. According to Tarantola the problem of finding regions of high probability can be alleviated the most through gaining knowledge of the aspects of the problem at hand prior to sampling efforts [16]. Efficient sampling of the high probability region is achieved through MC based sampling techniques which in the present case take advantage of Brownian-like walking motion inside the domain. Sampling algorithms employed in SMUQ are presented in the following sections .

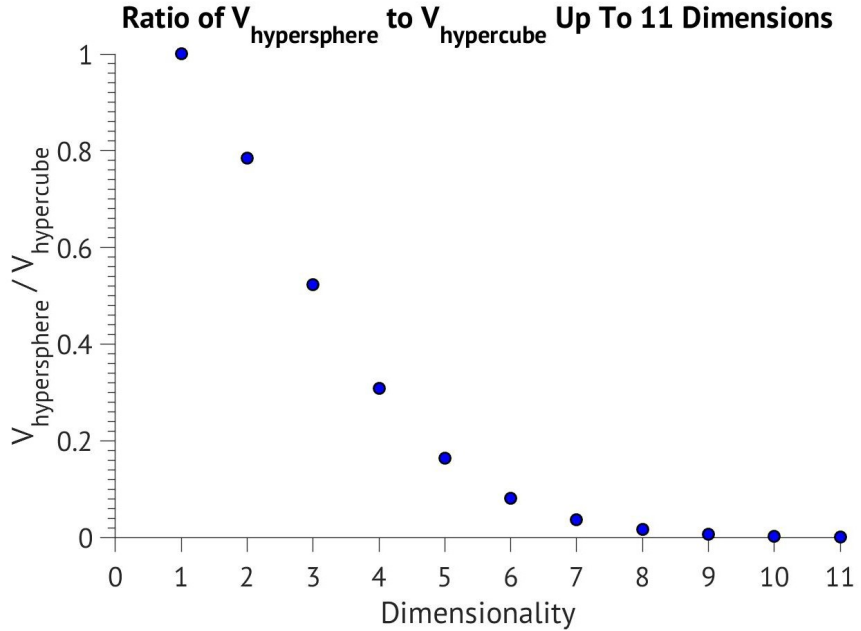


Figure 4.3: The probability of drawing a sample inside of a unit hypersphere that is inscribed inside of a unit hypercube at varying dimensions of up to 11–D [16].

4.2 Metropolis–Hastings Algorithm

A large class of Monte Carlo algorithms are based on the adherence to the properties of a Markovian chain. Successive samples in general sampling approaches may not be independent of sample history. However, if successive samples of a Monte Carlo method show dependence only on the previous sample drawn, the algorithm is then said to be an example of a Markov Chain Monte Carlo method [MCMC]. This property can be expressed as Equation 4.1 where it states that given a current sample $\boldsymbol{\theta}_i$, the past and future of the sample sequence are independent [54].

$$P(\boldsymbol{\theta}_{i+1} | \boldsymbol{\theta}_0, \dots, \boldsymbol{\theta}_{i-1}) = P(\boldsymbol{\theta}_{i+1} | \boldsymbol{\theta}_{i-1}) \quad (4.1)$$

One of the most utilized MCMC methods is the Metropolis–Hastings [MH] algorithm. The approach consists of a random Brownian motion sampler that is augmented by probabilistic selection methods. The final result is an algorithm that samples a target distribution in an efficient manner that follows the Markovian property. When sampling a general PDF $P(\cdot)$, the MH algorithm consists of the following steps:

1. First draw a random sample $\boldsymbol{\theta}_0$ from the target distribution such that

$$P(\boldsymbol{\theta}_0) > 0 .$$

2. Using a symmetric proposal PDF $Q(\cdot)$ centered about the previously accepted sample, draw a new sample $\boldsymbol{\theta}_p$ and then compute the probability $P(\boldsymbol{\theta}_p)$. This is demonstrated in Figure 4.4 for a 1-D example.
 3. Compute the statistic α using probability of previously accepted sample $P(\boldsymbol{\theta}_i)$ as well as the value $P(\boldsymbol{\theta}_p)$ as follows:
- $$\alpha = \frac{P(\boldsymbol{\theta}_p)}{P(\boldsymbol{\theta}_i)}. \quad (4.2)$$
4. Finally, decide whether to accept the proposed sample based on the value of the statistic computed in Equation 4.2. In the event that $\alpha \geq 1$, accept the sample outright and $\boldsymbol{\theta}_{i+1} = \boldsymbol{\theta}_p$. If $\alpha < 1$ then draw a number α_{test} from a uniform distribution of domain $[0, 1]$ and accept the sample if $\alpha_{test} \leq \alpha$. Otherwise, if the acceptance test fails, reject the sample and $\boldsymbol{\theta}_{i+1} = \boldsymbol{\theta}_i$.
 5. Repeat steps 2 through 4 until the distribution has been sufficiently sampled.

If non-symmetric proposal distributions are desired, the outlined MH algorithm must be adjusted by changing the computation of the α in Equation 4.2 to be that of Equation 4.3. In the equation below the probability $Q(\boldsymbol{\theta}_i, \boldsymbol{\theta}_p)$ is the probability of transitioning to $\boldsymbol{\theta}_p$ from the process sample location $\boldsymbol{\theta}_i$ according to the general proposal distribution $Q(\cdot)$, where as $Q(\boldsymbol{\theta}_p, \boldsymbol{\theta}_i)$ is the reverse case. It can be observed that when the proposal distribution is symmetric the proposal probability terms cancel and Equation 4.2 is retrieved. The remaining steps of the MH algorithm procedure are unaltered.

$$\alpha = \frac{P(\boldsymbol{\theta}_p) Q(\boldsymbol{\theta}_p, \boldsymbol{\theta}_i)}{P(\boldsymbol{\theta}_i) Q(\boldsymbol{\theta}_i, \boldsymbol{\theta}_p)} \quad (4.3)$$

The Metropolis–Hastings algorithm demonstrates two great advantages over standard random sampling of the entire domain. The acceptance of samples based on α forces the MH algorithm to prefer the sampling of high probability density regions and makes the progression of the Markov chain into regions of extremely low probability highly unlikely. This aspect is especially beneficial in higher dimensions where it was shown that the sampling domain may consist of only small regions of high probability. Second, the use of proposal distributions

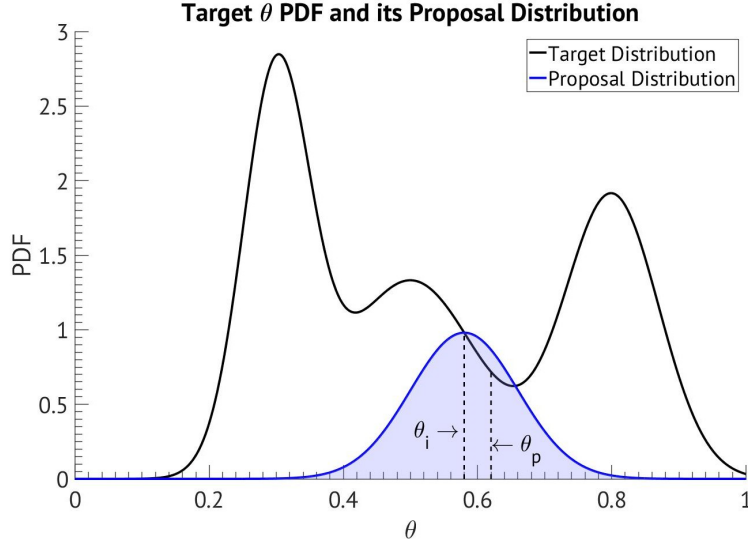


Figure 4.4: Proposal distribution (non-normalized here) sampling utilized during the sampling of the target PDF (normalized) with Metropolis–Hastings algorithm.

and the control over their span limits to a degree the number of points in the sampling domain that are drawn from any neighboring empty space. Instead, the proposal samples are drawn mostly from the region of high probability given that an appropriate choice for sampling distributions shapes has been made. The MH algorithm retains the Markovian property where the converged equilibrium solution is the PDF that is being sampled. According to Tarantola, the probabilistic rules in the MH approach that are used to augment the random walk sample a target distribution are the most efficient [16].

In addition, the method behind the computation of the acceptance statistic in Equations 4.2 and 4.3 enables a great simplification to the computation of the posterior PDF in Chapter 3. Any generic PDF can be re-expressed as in Equation 4.4 where C is a normalization constant and $f(\boldsymbol{\theta})$ is a non-normalized PDF.

$$P(\boldsymbol{\theta}) = \frac{f(\boldsymbol{\theta})}{C} \quad (4.4)$$

Consequently, because both the drawn and proposal samples are from the same target distribution, the ratio of their respective sample probabilities in the equations for α above reduce to the ratio of the probabilities drawn from the non-normalized distribution as shown in Equation 4.5. Therefore, when sampling the

posterior distribution in Bayes' theorem, the computation of the normalization term can be omitted and individual non-normalized posterior PDF sample values take on the form shown in Equation 4.6 which is used in the computation of α parameter.

$$\frac{P(\boldsymbol{\theta}_p)}{P(\boldsymbol{\theta}_i)} = \frac{f(\boldsymbol{\theta}_p)}{C} \frac{C}{f(\boldsymbol{\theta}_i)} = \frac{f(\boldsymbol{\theta}_p)}{f(\boldsymbol{\theta}_i)} \quad (4.5)$$

$$f(\boldsymbol{\theta}) = L(\mathbf{y} = \mathbf{D} | \boldsymbol{\theta}, M) P(\boldsymbol{\theta} | M) \quad (4.6)$$

Prior to initiating the MH sampling algorithm, the form of proposal PDFs must be chosen. The design of these PDFs is however not always clear and the choice has a significant impact on the progression of the chain. In Venturi [49] the effect of changing the standard deviation σ of a Gaussian proposal PDF was investigated on a generic 1D multi-modal distribution. Three cases in total were examined where in each case a gaussian proposal with a standard deviation of σ , $\sigma/2$, and $\sigma/4$ was tested. The plots of the results obtained are reproduced here for convenience in Figure 4.5. It was observed that when proposal distributions are made either too large or too small the chain does not mix well. In the former case the algorithm rejects numerous samples before accepting another, while in the latter case new samples are accepted often but only very near the previous sample due to the narrow proposal PDF, which results in slow exploration of the sampling space. Hence it was concluded in Ref. [49] that an intermediate form must be chosen where chain history resembles that of the intermediate case shown in (c) and (d) of Figure 4.5. A common metric of the quality of chain mixing is the acceptance ratio and is based on the number of times the acceptance test passes during the evolution of the Markov chain. While low acceptance rates denote a Markov chain that is stationary on most attempts like in (a) and (b), a high acceptance rate is indicative in most cases of a chain that accepts copious number of samples very close to previously accepted trials as shown in case (e) and (f) of Figure 4.5. Hence the behavior observed in (c) and (d) is mainly desired.

4.3 Delayed Rejection–Adaptive Method MCMC

Although much more preferable than brute force sampling of the entire PDF domain, improvements to the Metropolis–Hastings were introduced meant to enhance the method's ability to quickly converge to the equilibrium solution. As part of SMUQ, the basic MH algorithm was augmented with the Delayed Rejec-

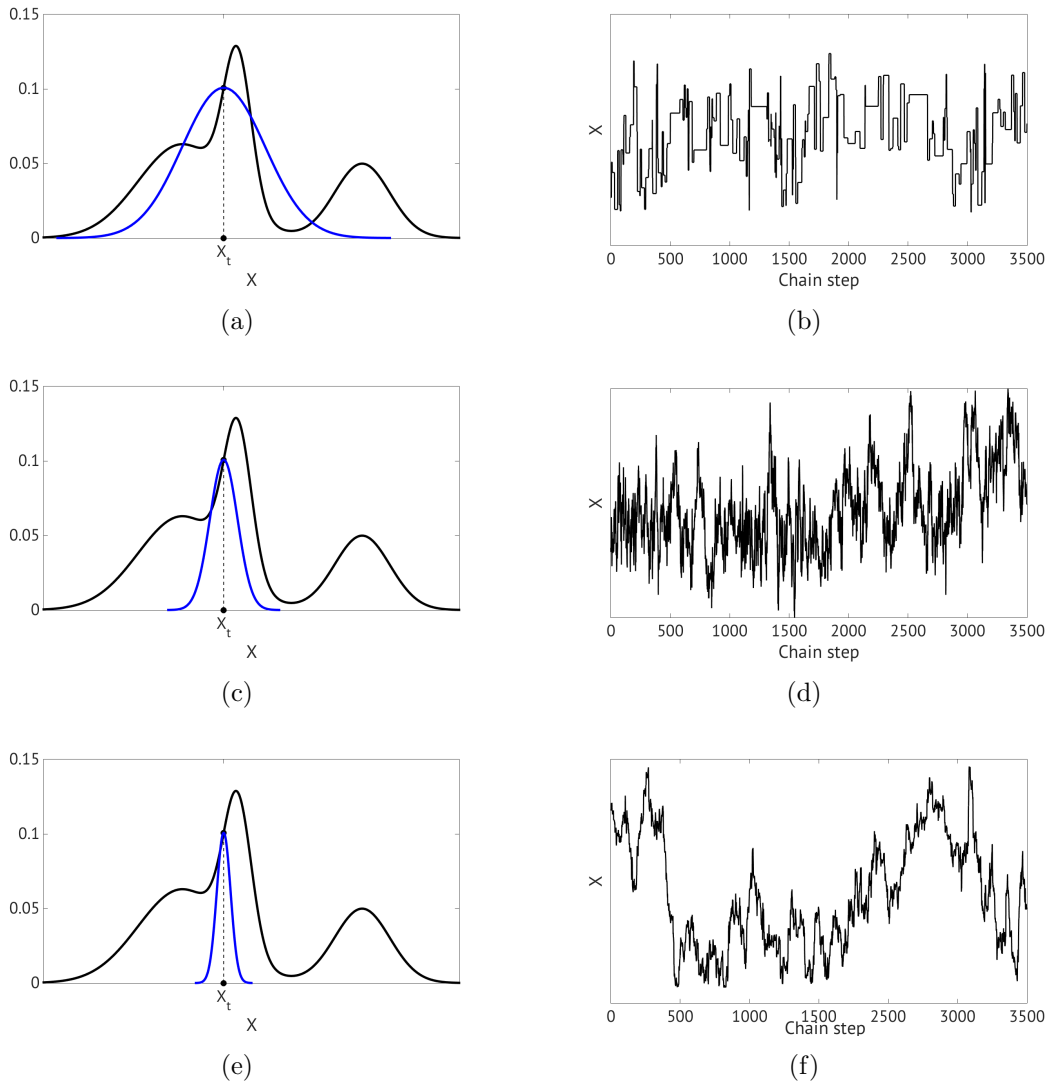


Figure 4.5: Sampling histories of a generic 1D PDF using Metropolis–Hastings algorithm where proposal normal distributions with standard deviations of σ (a), $\sigma/2$ (c), and $\sigma/4$ (e) were used with corresponding chain histories shown in (b), (d), and (f) respectively [49].

tion and Adaptive Method schemes which are summarized and examined in the following subsections.

4.3.1 Delayed Rejection

The Delayed Rejection [DR] method alters the approach with which individual samples are taken and accepted. In the original MH algorithm, a sample is drawn from a proposal distribution and if the acceptance test is a pass, the new sample point is recorded and the chain advances. Whereas if the test fails, the last accepted sample is re-recorded and the chain stays stationary. The DR method devised by Green and Mira [55] adjusts this selection process by introducing additional proposal sampling attempts prior to rejection. When a sample from the proposal distribution fails the acceptance test, instead of recording $\theta_i = \theta_{i+1}$ additional attempts are made with smaller proposal PDFs with each successive re-trial. When the proposal distributions are chosen to be Gaussian PDFs, the process corresponds to a shrinking covariance matrix C with each trial j , starting with the first trial $j = 1$, as given by Equation 4.7 where γ is called the DR parameter and is recommended be set to 0.5 in most cases by the authors of the method.

$$C_{p,j} = C_{p,j=1} \times \gamma^{j-1} \quad (4.7)$$

The formulation for the acceptance statistic α is altered from that in Equation 4.3 to account for the additional generic number of DR steps. The generic expression is long and can be found in Ref. [55]. However, if symmetric distributions are used to construct the proposal distribution, the computation of the acceptance statistic is greatly simplified and can be found in a separate work by Mira [56] which also details the algorithm's implementation.

The DR procedure is visualized in Figure 4.6 for a 1D target PDF where two re-trial steps are allowed with the recommended DR parameter setting. The first DR step consists of generating a sample $\theta_{p,1}$ from the Gaussian proposal distribution where the σ parameter is unchanged. If the first sample fails the acceptance test, the proposal distribution is redrawn where the σ is now reduced by half and a new candidate $\theta_{p,2}$ is drawn from the updated proposal PDF. If the acceptance test again does not pass, the proposal distribution is redrawn again where the standard deviation is again halved and from it a candidate $\theta_{p,3}$ is obtained. In general if the acceptance criteria is again not met, the chain remains stationary

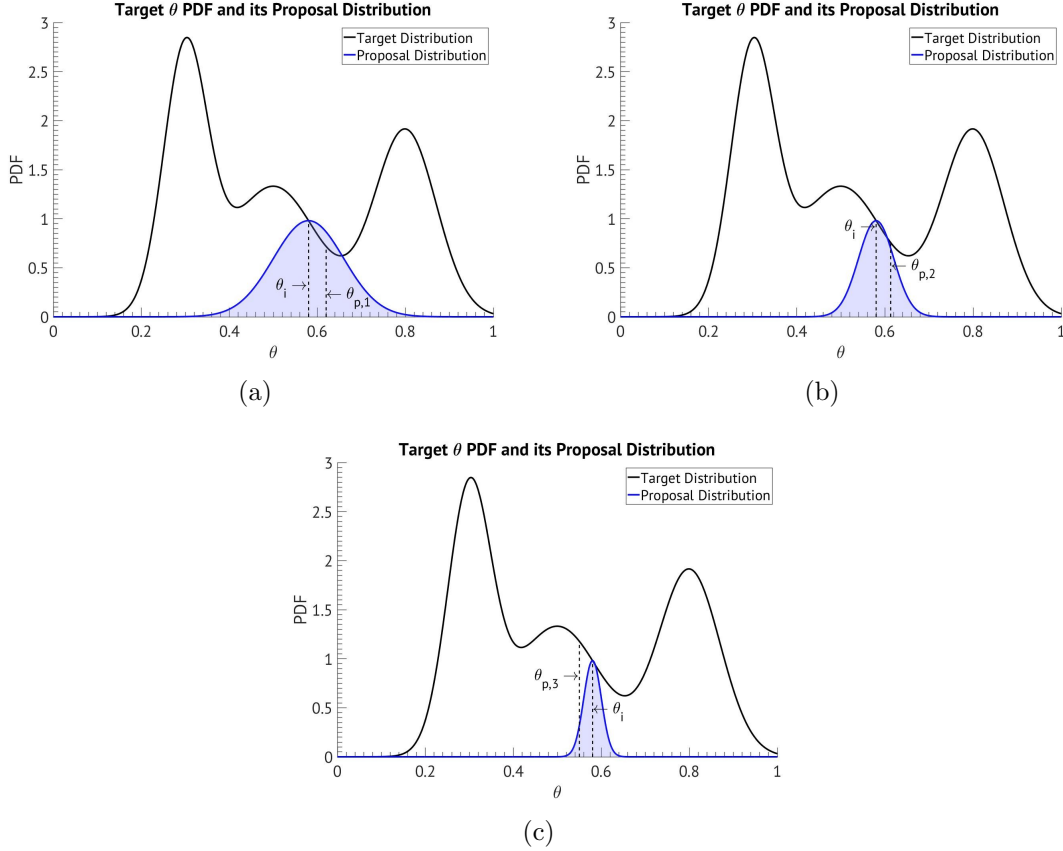


Figure 4.6: The progression of the 3-step Delayed Rejection method where the DR parameter is set to 0.5 and both first (a) and second (b) DR steps do not yield an accepted sample.

and $\theta_i = \theta_{i+1}$ is recorded. However, in Figure 4.6 (c) it can be seen that the new sample corresponds to an automatic acceptance according to the procedure outlined in the previous subsection and thus $\theta_{p,3} = \theta_{i+1}$ is recorded. Indeed a three step DR approach is highly desirable as the proposal distribution of the first attempt can be on purpose made to cover large parts of the domain. The benefits of doing so include fast initial exploration of the domain if the sampling process starts in regions of low probability as well as the ability to capture multi-modal behavior in the regions of high probability density to a degree. The second step can be thought of as a local exploration step that comes after the first step's failure to find a far off region of higher probability. The third step with this design is consequently the “fine-tuning” step of the sampling process which is beneficial when the target PDF consists of very narrow regions of high probability density.

4.3.2 Adaptive Method

Whereas the Delayed Rejection method adjusts the sampling procedure to allow for more trials to be carried out prior to rejection, the Adaptive Method [AM] devised by Haario et al. [57] augments the original MH algorithm by modifying the proposal distribution during sampling. Specifically, the AM methodology focuses on the use of Gaussian proposal PDFs where the covariance matrix is updated based on the accepted sample history. The procedure for the implementation of this augmentation begins by first defining a Gaussian proposal distribution with a positive definite covariance matrix C_0 based on prior knowledge of parameters. The MH algorithm is allowed to explore the target PDF using the pre-defined proposal normal distribution for a number of samples until step number n_{preAM} is reached; this interval constitutes the "non-adaptation" period. Once a predetermined number of chain samples have been obtained, the AM procedure uses the recursive formula in Equation 4.8 to update the proposal covariance matrix based on past recorded samples. The length of the non-adaptation period can be set at investigator's discretion and in Ref. [57] it was stated the the covariance matrix should be updated at regular small intervals instead of at every transition step.

$$C_{i+1} = \frac{i-1}{i} C_i + \frac{s_d}{i} (i\bar{\boldsymbol{\theta}}_{i-1}\bar{\boldsymbol{\theta}}_{i-1}^T - (i+1)\bar{\boldsymbol{\theta}}_i\bar{\boldsymbol{\theta}}_i^T + \boldsymbol{\theta}_i\boldsymbol{\theta}_i^T + \epsilon I_d) \quad (4.8)$$

In the equation above the quantities are defined as follows: the barred quantities $\bar{\boldsymbol{\theta}}_i$ and $\bar{\boldsymbol{\theta}}_{i-1}$ represent the means of past i and $i-1$ (excluding the most recently accepted) samples, C_i and C_{i+1} are respectively current and updated covariance matrices, ϵ an extremely small factor that prevents together with identity matrix I_d singular covariance matrices, and s_d is a scaling factor recommended to be set to $s_d = 2.4^2/d$ by the authors of the method where d is the number of dimensions. One of the main benefits of the method is that it is possible to start with a diagonal covariance matrix for the proposal distribution and then allow the AM algorithm to gradually introduce correlation between parameters during sampling based on the history of the chain. As demonstrated in Figure 4.7, the initial covariance matrix in (a) is diagonal and therefore parameters are independent. With chain progression the covariance matrix is updated to introduce correlation between the two parameters from (a) through (c) resulting in a distribution that is rotated in its orientation as well as slightly elongated in (c).

The dependence on past samples of the AM algorithm breaks the Markovian property of the original MH chain as well as its reversibility. However, the authors

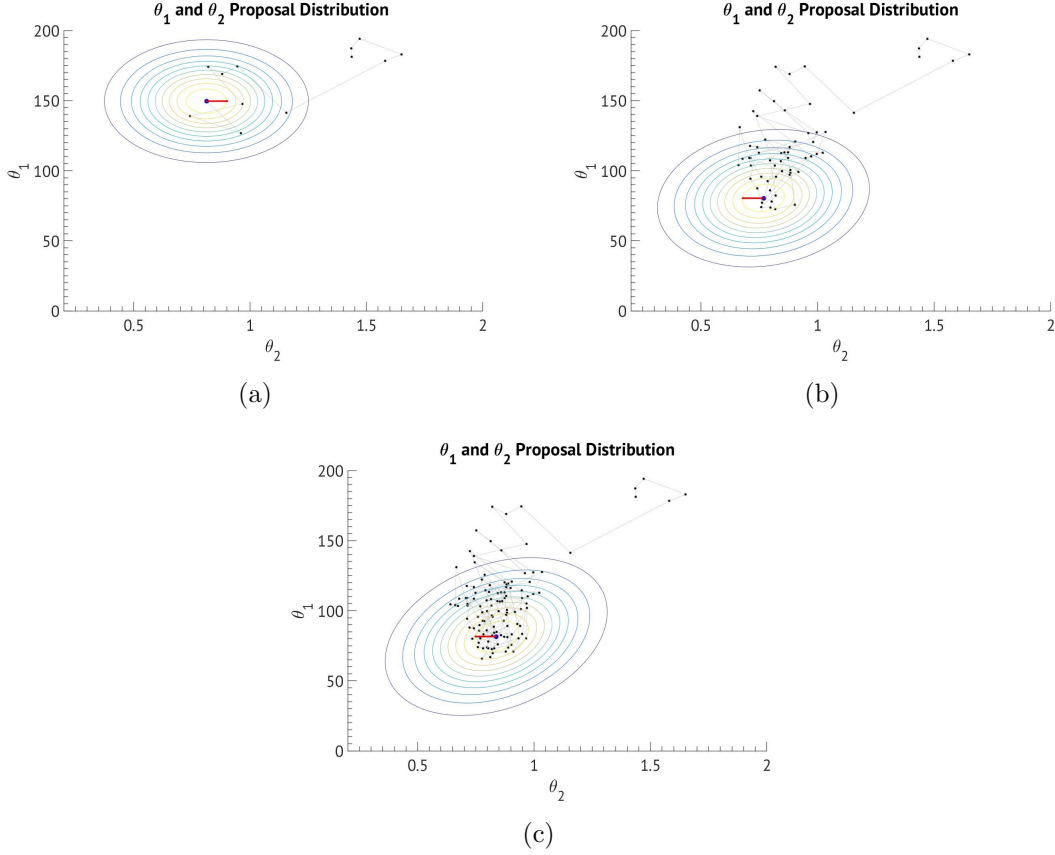


Figure 4.7: Evolution of proposal Gaussian distribution contours due to the updating of the covariance matrix with the AM algorithm starting with (a) and progressing to (c) where chain history is shown in each tile.

of the method had proven that given the satisfaction of certain properties, which in the case of the work contained in this thesis are true, the equilibrium solution will still correspond to the target PDF being sampled.

4.3.3 DRAM – DR and AM Combined

Both Delayed Rejection and Adaptive Method algorithms aim to improve the convergence ability of the MH algorithm by altering the basic approach taken to aspects of the sampling distributions and sample drawing procedures. In their work, Haario et al. [58] combined the two approaches into a single method called DRAM and proved its validity when sampling a target probability distribution function. The procedure is a logical extension of both methods. In the first attempt to sample the target distribution, an updated proposal covariance matrix

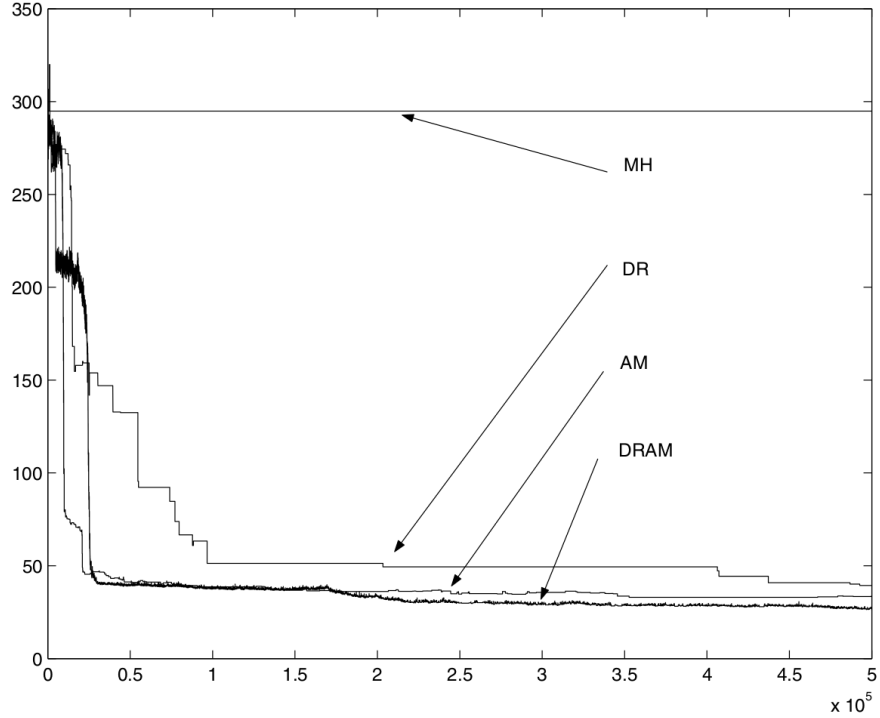


Figure 4.8: Performance comparison of base MH and MH augmented with DR, AM, and DRAM algorithms where pooled sums of the squared residuals vs. number of steps were plotted by the authors of Ref. [58] for a PDF sampling test case.

C_i is generated based on previous $i - 1$ samples. A sample is then generated from a normal distribution located at the current process location using the generated covariance matrix. In the event that the sample does not satisfy the acceptance criteria, the DR methodology is employed where successive proposal distributions are drawn at the same process location using scaled versions of the generated covariance matrix C_i as shown in Equation 4.7. In addition to its formulation, the authors of the DRAM algorithm also conducted a thorough study of its performance and compared it against the base MH approach as well as the DR and AM augmented versions separately. The results of one of those studies is reproduced in Figure 4.8 where a target PDF was sampled and the pooled sums of the squared residuals vs. simulation time were plotted. Both DR and AM methods alone showed superior performance over the base MH algorithm. In addition, results corresponding to the DRAM approach were better than for both AM and DR separately thanks to the interaction between both methods.

4.3.4 PID Driven DRAM

The quality of results obtained using MCMC based methods when sampling a target probability distribution depends on the quality of mixing present in the transition history of a chain. The quality of the obtained chain in turn can be deduced from the overall acceptance rate for which an intermediate value is vital. In the case of MH algorithm augmented with the DRAM approach in the present thesis, an acceptance rate of 50% is desired.

The acceptance rate statistic in the case of MH+DRAM algorithm can be controlled through two choices, initial proposal distribution covariance matrix and the value of the DR parameter. In the case of the covariance matrix with the recommended value for the DR parameter, an initial proposal that covers extremely large or small regions of the sampling domain may yield acceptance rates that may be small or large respectively based on the target distribution to be sampled; the AM method will not completely amend poorly chosen initial proposal distributions. Proper proposal distributions with a constant DR parameter that yield a desired acceptance rate are problem specific and are difficult to determine apriori. In the case of improperly mixing chains the initial proposal distributions must be adjusted in an iterative manner and sampling efforts restarted; this effort grows much more difficult with increasing input dimensionality. In the case of computationally expensive models this approach towards fixing the mixing of the transition chain is extremely wasteful.

The author of this thesis and the author of Ref. [49] chose to focus on the control of the DR parameter setting in order to fix sampling efforts that yield undesired behaviors. The approach that was devised involves the control of the value of the DR parameter with a PID controller that takes as input the local acceptance rate of past k number of chain samples and outputs a DR parameter value that will drive the local acceptance rate towards the desired 50%; the overall acceptance rate will be driven to the 50% target by extension. The procedure involves the following two ideas:

- Define the initial proposal distribution covariance matrix to be a diagonal matrix where each independent normal distribution spans over a very large portion of the corresponding input sampling distribution domain. In the case of this thesis, the σ per each original independent normal proposal distribution was set to be 1/12 of the input distribution range.

- Prior to drawing the first sample for the first DR step $j = 1$ for all individual transition attempts i , calculate the new DR parameter using a PID controller where the input is the local acceptance rate based on the last k transitions of the chain history, the goal is a local acceptance rate of 50%, and the output control variable is a new DR parameter value.

The AM method is unlikely to reduce the span of an initial proposal distribution by a large factor. Due to this behavior of the AM portion of DRAM as well as the fact that the first step of the DR parameter does not adjust the covariance matrix in any way, selection of a large initial proposal distribution means that the sampling scheme will retain its ability to capture multi-modal behaviors throughout the sampling procedure no matter the behavior imposed by the PID controller on the DR parameter. The random walk is initially also likely to take very bold steps and arrive in the vicinity of the region of high probability density if the starting point is in a region of small probability.

The expression for the PID controller implemented inside of SMUQ was obtained by first taking the derivative of both sides of Equation 4.9 where e is the error value and u is the control variable. The discrete form of the resulting expression was then derived and solved for the value of the new DR parameter which is in the current case the control parameter.

$$u(t) = K_p e(t) + K_i \int_0^t e(\tau) d\tau + K_d \frac{de(t)}{dt} \quad (4.9)$$

The alternate algorithm for the PID controller removes difficulties caused by the integral term in typical implementations; they are extremely susceptible to error wind-up complications. The number of past transitions from which the local acceptance rate is computed is an input that is left to be chosen at the discretion of the investigator. In the present case, past 100 transitions are considered but the number can be chosen to be larger if a more gradual control of the DR parameter is desired. Finally, the PID controller can be turned on immediately after the start of the chain where the local acceptance rate will be computed using information from all transitions made until sample $i > k$ is reached. However, doing so is not advised as the PID controller response can be chaotic when the chain is still in a low probability region of the target PDF; local acceptance ratio is likely to be high and show erratic trends. The PID controller in this work is instead turned on by default at the same chain step where the covariance of the

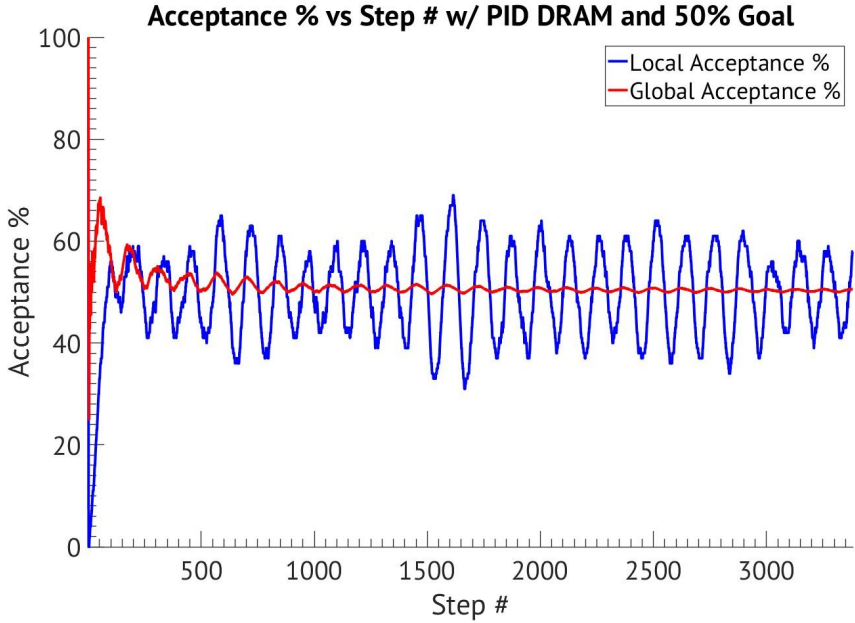


Figure 4.9: Local and cumulative acceptance rate histories recorded during a sampling run of a PDF using DRAM PID extension of the MH algorithm.

proposal distribution begins to be updated by the AM component of DRAM. The controller gains were obtained by running a sampling run on a target PDF with the basic DRAM algorithm and then changing the DR parameter half way through the procedure. Using MATLAB, a PID controller response was then fitted to the local acceptance rate history plot where the gains were found to be $K_p = -2.2$, $K_d = 0.0$, and $K_i = -0.1$. Although these values were found using a test case, an exact steady state value of the target acceptance rate is not critical and an approximate behavior suffices. A steady state error as well as oscillations around the desired acceptance value are tolerable as long as they do not deviate significantly from the target.

An example of the resulting behavior of a sampling run where PID DRAM was utilized is shown in Figure 4.9; local acceptance and overall acceptance rates are plotted versus the step number. The local acceptance rate is shown to oscillate about the target acceptance while the overall acceptance quickly converged to the desired value. The ergodicity properties of the PID extended DRAM algorithm are yet to be studied along with the best values for the number of transitions to consider in the calculation of the local acceptance rate. These aspects are planned to be explored in future efforts and are beyond the scope of the current work.

4.4 Sampling of Multimodal PDFs

Some probability distribution functions may show severe multimodal behavior where multiple peaks in the PDF can be identified. This situation is likely to be encountered during calibration outlined in Chapter 3 when the dimensionality of the input model parameter space is large. In such occasions, the walking DRAM algorithm can encounter difficulties in sampling the modes of the distribution especially if they are separated by regions of very low probability. The proposed wide proposal distributions for the PID DRAM extension of the MH algorithm are able to a degree alleviate multi-modal behavior.

If a posterior distribution is known to consist of a number of modes that will not be sampled adequately by the PID DRAM algorithm, two possible approaches to remedy the problem have been implemented in SMUQ. One of these solutions involves the method of simulated annealing detailed by Tarantola [16]. The method aims to replicate the physical process of annealing encountered in metallurgy during sampling where artificially a larger number of samples are accepted; the artificial push to accept more samples decays overtime. The second option on the other hand is preferred over simulated annealing, and it consists of running multiple sampling chains in parallel with different starting points and evolution. This approach was studied well by Gelman and Rubin [59] where the sampling performance of a target multi-modal distribution with the Gibbs sampling algorithm was improved with the use of multiple sampling chains.

4.5 High Posterior Density Regions

The model calibration problem posed in Chapter 3 is solved by using above approaches to sample the posterior probability distribution. The marginalization of the sampled posterior PDF returns probability distributions corresponding to each model parameter that express updated knowledge and uncertainty concerning each respectively. The propagation of parameter posterior PDFs through the statistical forward problem in addition to the quantified uncertainty due to model inadequacy and data inaccuracies yields a joint output probability distribution $p(\mathbf{y}|\mathbf{D}, M)$ for desired quantities of interest.

In the study done by Oliver et al. [19] it was made evident that calibration procedures strive towards making model output match calibration data as best as

possible . However, there is no guarantee that model output will match exactly data that are newly aquired or those that were used during calibration. In the current context, the probability of obtaining data \mathbf{D} based on the output PDF may not be substantial even after calibration. The authors of Ref. [19] recommended the use of High Posterior Density [HPD] credibility regions instead of a visual inspection for a proper metric of whether observed data are a plausible outcome of the calibrated output distribution; HPD credibility regions are thoroughly discussed by Box and Tiao [60]. It was stated in the study that the HPD region “is the set for which the probability of belonging to S is β and the probability density for each point in S is greater than that of points outside S ” [19]. The formulation for the β statistic utilized here takes the form of Equation 4.10 where \mathbf{y} are model output quantities for which output PDFs were obtained through the solution of the statistical forward problem and \mathbf{Y} are the corresponding observed values.

$$\beta = \int_S p(\mathbf{y}|\mathbf{D}, M) d\mathbf{y}, \quad \text{where } S = \{\mathbf{y} : p(\mathbf{y}|\mathbf{D}, M) \geq p(\mathbf{Y}|\mathbf{D}, M)\} \quad (4.10)$$

The procedure for obtaining HPD intervals and the value of the β statistic can be given physical intuition by using Figure 4.10. The first step of the visual procedure involves drawing a horizontal line through the point of global maximum of the pictured PDF. Once the line is drawn, it is incrementally shifted towards the x-axis. The horizontal line will begin to intersect the black PDF outline and will form intervals inside of its interior. The integration of the area underneath the PDF curve inside the newly defined intervals, where in the case of Figure 4.10 the intervals are formed by points S_1 and S_2 in addition to S_3 and S_4 , will yield the value of β for the current location of the horizontal line with the corresponding intervals forming the β value HPD regions.

In the present case scenario where the plausibility of observed data given the calibrated output PDF is being investigated, a slightly altered routine than the one above is implemented. Instead of finding HPD regions based on a pre-determined value of β , HPD regions are sought after that both include recorded data for the observable quantity under consideration and minimize the magnitude of the parameter β . In terms of the visualization procedure exercised previously, a horizontal line is drawn at the global maximum of the output PDF for an observable quantity which is then shifted down until it intersects with a data point. Once both are in contact, the parameter β is computed and the quality of the results

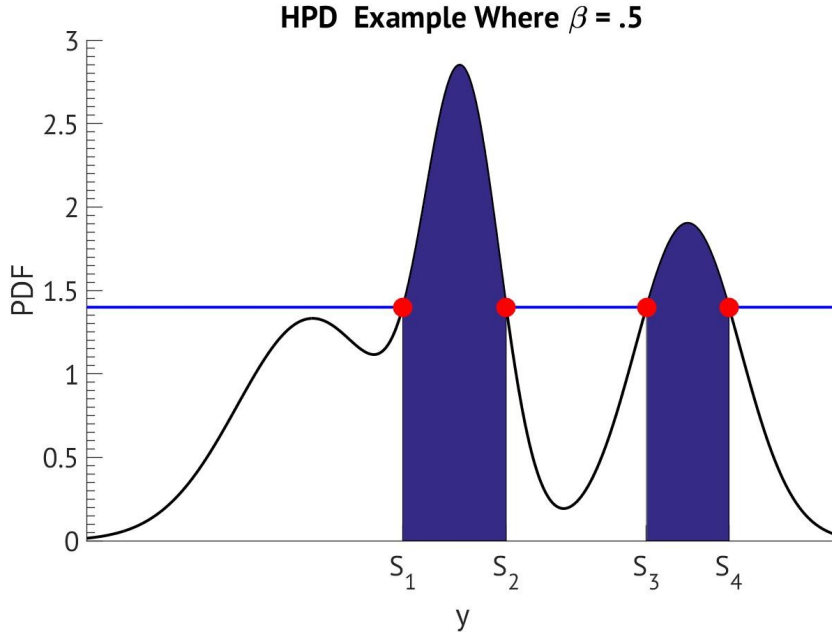


Figure 4.10: An example of 50% HPD regions where the areas in dark blue are the regions, black line is a generic output distribution, and red markers are locations where the horizontal line intersects the black line.

of the calibration are ascertained based on the value of the parameter. It can be easily deduced given the current discussion that in the event where $\beta = 0$ the most probable predicted output from the output PDF aligns with validation data for the observable quantity; model is able to replicate data well. However, if the value of the parameter is near unity, the model is unable to replicate the physical phenomena involved.

The outlined procedure provides a rigorous approach with which the ability of a calibrated model to replicate phenomena under consideration can be evaluated. The computation of HPD intervals is consequently used in Chapter 5 to assess the quality calibration results.

Chapter 5

Results

In the present work calibration of the VISTA material database using Bayesian inference is performed using material temperature flight data collected during the Apollo 4 test flight. The process is carried out using an in-house developed code dubbed SMUQ that implements methods discussed in Chapters 3 and 4 to arrive at the solution of the statistical inverse problem. Uncertainty quantification of calibrated results is done by forward propagating parameter PDFs as well as non-parametric sources of uncertainty through the statistical forward problem.

The contents of this chapter are organized as follows. First the flight scenario to be studied is detailed along with a discussion of obtained data. A sensitivity analysis is then done for the Apollo 4 scenario and results are reviewed and used to reduce the dimensionality of the uncertain input parameter space. In addition, problem dependent aspects of calibration such as the error form assumption, likelihood formulation, and input parameter priors employed throughout the remainder of this thesis will be given. Calibration of the VISTA model is done along with uncertainty quantification in the final sections of this chapter with both synthetic and flight data.

5.1 Flight Scenario and Data

Data used in the calibration of uncertain VISTA model parameters was obtained by digitizing temperature profile plots recorded during the Apollo 4 test flight [15]. Objectives of the mission included the study of the heat-shield ablator performance when exposed to the conditions generated during super-orbital entry velocities that future manned Apollo flights would experience on their trans-lunar return trajectory. The material temperature history consists of thermocouple measurements collected at different depths in two separate plugs placed in the vehicle's aft heat shield. Original plots of temperature profiles recorded at Plugs

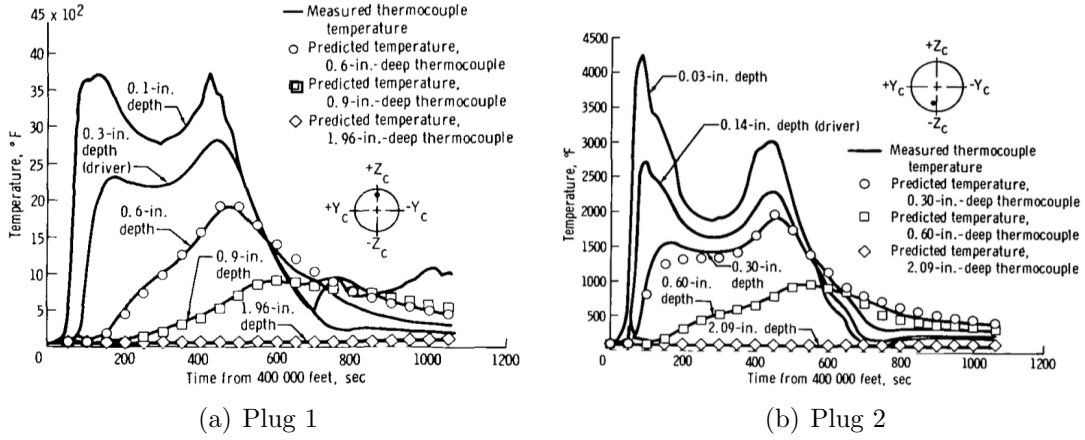


Figure 5.1: Material temperature data recorded by thermocouples located in Plug 1 (a) and Plug 2 (b) at different depths in the aft heat shield of Apollo 4 [15].

1 and 2 are reproduced in Figure 5.1 as well as their respective locations on the vehicle's aft heat shield. The scenarios in the figure begin once the vehicle had reached an altitude of 400,000 ft. and continue for over 16 minutes past the start of the recordings. The plug shown to be located 50 inches away from the center on the pitch plane will throughout this work be referred to as Plug 1 while the plug located near the area of maximum heating will be referenced to as Plug 2. Of the available data, temperature recorded by the front most thermocouple is used as the thermal boundary condition with the TC driver method; the sample length is appropriately re-scaled where the new origin coincides with the location of the thermocouple driver. This approach removes the need to model the highly complex flow field environment during hypersonic re-entry as well as the need to model recession of the material. Temperatures recorded at deeper depths of the charring ablator where significant changes were observed are then used as data during calibration.

Data obtained during both flight and ground facility experiments are subject to uncertainties caused by contamination, diagnostic measurement tools, post-processing of raw data, etc. In this work two possible sources of data error are identified: digitization of data and instrument measuring inaccuracies. In general, AVCOAT material performance data recorded during atmospheric re-entry flights are difficult to obtain in raw form. The availability of plots of temperature profiles for handful of plugs of the Apollo 4 flight made it possible to digitize data, using one of the freely available tools on the internet, for use in the calibration of VISTA

model parameters. However, process of digitization and accuracy of the results depends on the quality of images available for analysis. The source of the plots used in this work was a low-quality online scan of printed material from 1970s. Flight data moreover are affected by measurement instrument accuracy which results in noise present in final readings. Thermocouple instruments also suffer from a slight delay in their temperature measurements of materials due to the thermal lag effect [61].

Although referenced, work containing information detailing the accuracy of the instrumentation onboard the Apollo 4 flight could not be accessed [62]. A minimum uncertainty threshold of 10% error is instead assumed on obtained data which encapsulates errors due to both data digitization and instrumentation accuracy. These sources of error are expected to be the largest source of experimental error in obtained data.

The above possibilities form experimental uncertainty the magnitude of which in basic forward propagation approaches to uncertainty quantification must be determined apriori. On the other hand in this work, experimental uncertainty combined with modeling error constitute a separate parameter to be calibrated. This parameter encapsulates both experimental and model errors and makes either indistinguishable from the other. It has been established that the confidence in data cannot be lower than an error of 10%, and it will serve as the lower bound during calibration, corresponding to the case of no structural model inadequacies present.

5.2 Sensitivity Analysis of VISTA in Apollo 4 Scenario

Prior to the calibration exercise, a sensitivity study is carried out with the method of Sobol and computation of Pearson correlation coefficients; temperature of the charring ablator is designated as the quantity of interest. The model parameter space in the sensitivity study is explored using a quasi-Monte Carlo scheme paired with the low discrepancy Sobol sequence and 25800 and 14340 model runs for the computation of Sobol indices and Pearson correlation coefficients respectively; determination of converged Pearson correlation coefficients requires a smaller number of model runs. The algorithms implemented for both approaches are susceptible to numerical errors when variance in the output is extremely small compared to output sample values. Figures containing the results of the study, therefore, be-

Table 5.1: VISTA Uncertain Parameters and Their Sampling Distributions.

| Input Parameters | Parameter | Sampling Distribution |
|-----------------------------------|------------------------|-----------------------|
| Virgin State Thermal Conductivity | $\lambda_{virgin\ P1}$ | $U[0.06, 0.15]$ |
| | $\lambda_{virgin\ P2}$ | $U[400, 650]$ |
| | $\lambda_{virgin\ P3}$ | $U[200, 800]$ |
| Char State Thermal Conductivity | $\lambda_{char\ P1}$ | $U[0.8, 1.8]$ |
| | $\lambda_{char\ P2}$ | $U[1500, 2700]$ |
| | $\lambda_{char\ P3}$ | $U[600, 1600]$ |
| First Reaction Pre-Exponential | A_{r1} | $10^{U[7,10]}$ |
| Second Reaction Pre-Exponential | A_{r2} | $10^{U[7,10]}$ |
| Third Reaction Pre-Exponential | A_{r3} | $10^{U[7,10]}$ |
| Virgin State Porosity | ϕ_{virgin} | $U[0.6, 0.8]$ |
| Virgin State Permeability | K_{virgin} | $10^{U[-12,-9]}$ |
| Char State Porosity | ϕ_{char} | $U[0.8, 0.95]$ |
| Char State Permeability | K_{char} | $10^{U[-12,-9]}$ |

gin at the point in time where the sample output variance exceeds approximately 0.01K. The TC Driver boundary condition takes the form of data collected by the frontmost thermocouple in Plugs 1 and 2 shown Figure 5.1. The sensitivity study is performed simultaneously for both plugs at two thermocouple locations closest to the TC driver per plug.

Input parameters to be varied are shown in Table 5.1. Select few parameters, namely the thermal conductivities of virgin and char states, are functions of temperature. A function of the form of Equation 5.1 is utilized to approximate these relationships.

$$y(x) = ae^{-(\frac{x-b}{c})^2} \quad (5.1)$$

This function form is chosen due to the original thermal conductivity temperature relationships being obtained with Gaussian fits on existing experimental data [14]. Although heat capacity of the ablating material is an important parameter in general, it has been excluded from the analysis of this work. In the presence of measurement errors it is not possible to calibrate simultaneously thermal conductivity and heat capacity of virgin and char states of an ablating material due to their strong, mutual correlation [29]. Greater confidence in the original values of the heat capacity was also expressed by the authors of this work apriori than for the values of thermal conductivity. Input parameter distributions were also forward propagated through the statistical forward problem in order to determine uncertainty in the model output prior to calibration.

5.2.1 Sensitivity Results

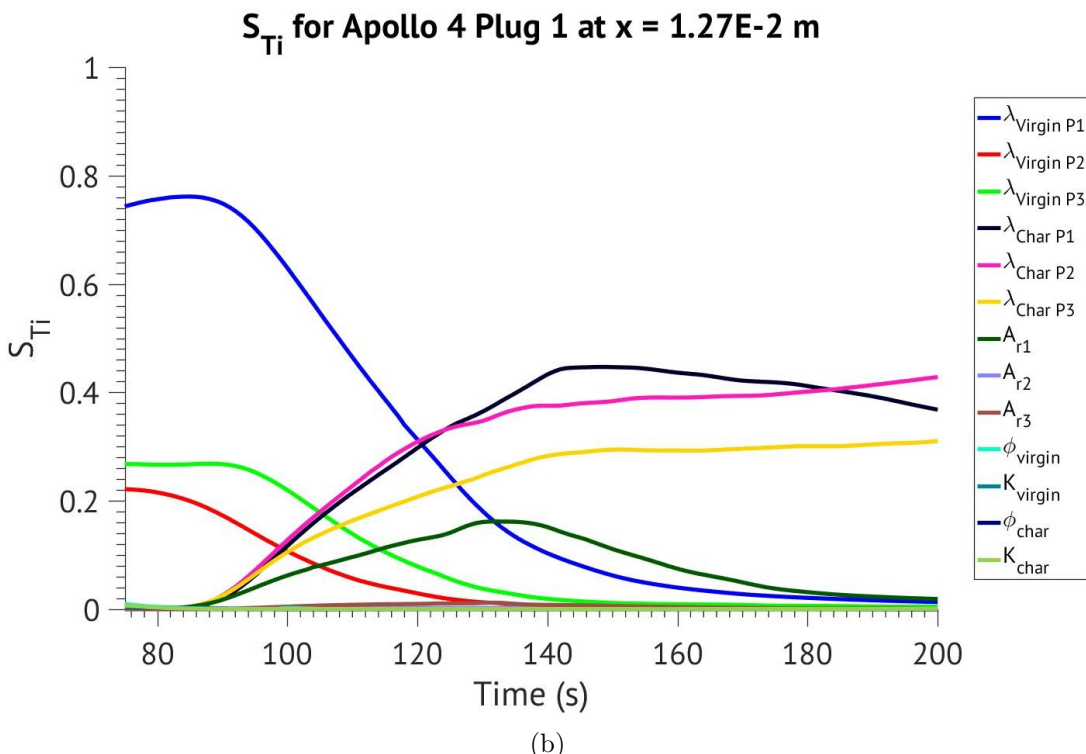
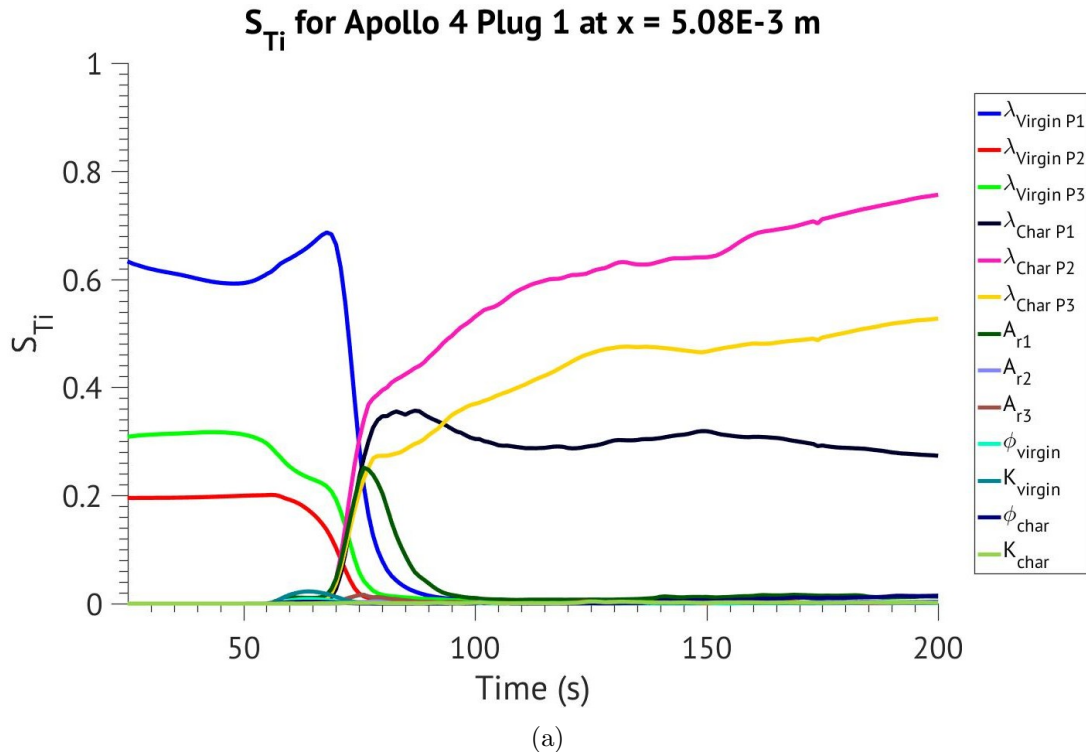


Figure 5.2: Results of the sensitivity study of VISTA performed with the method of Sobol for thermocouples located in Plug 1 of Apollo 4 flight.

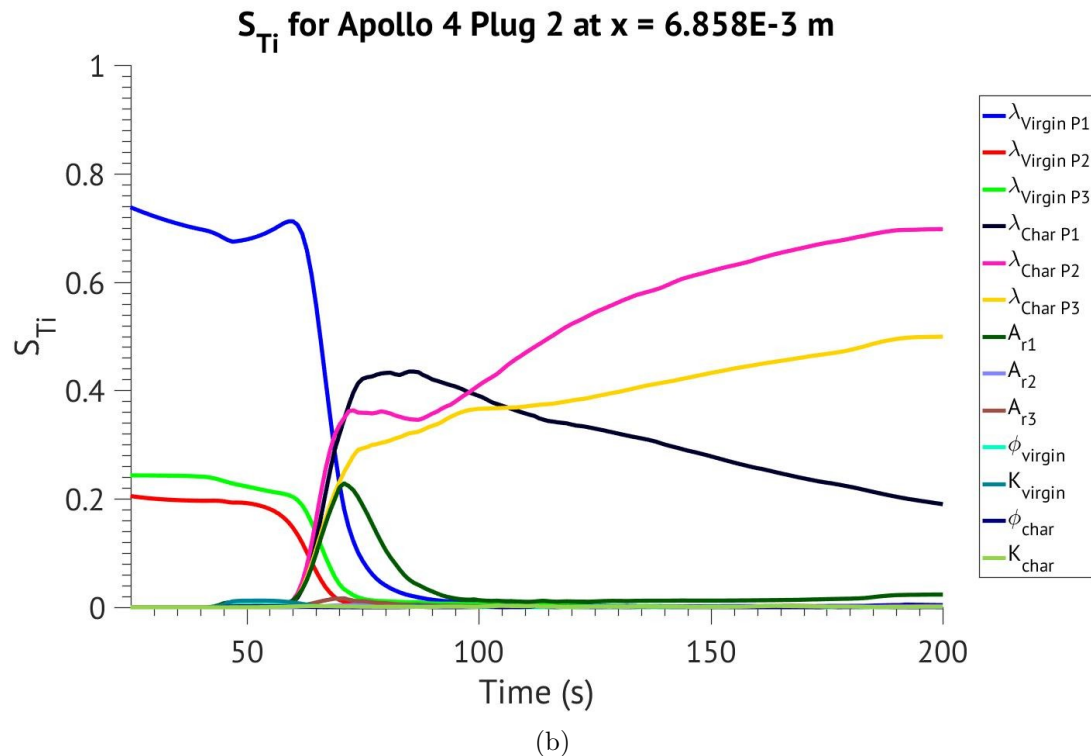
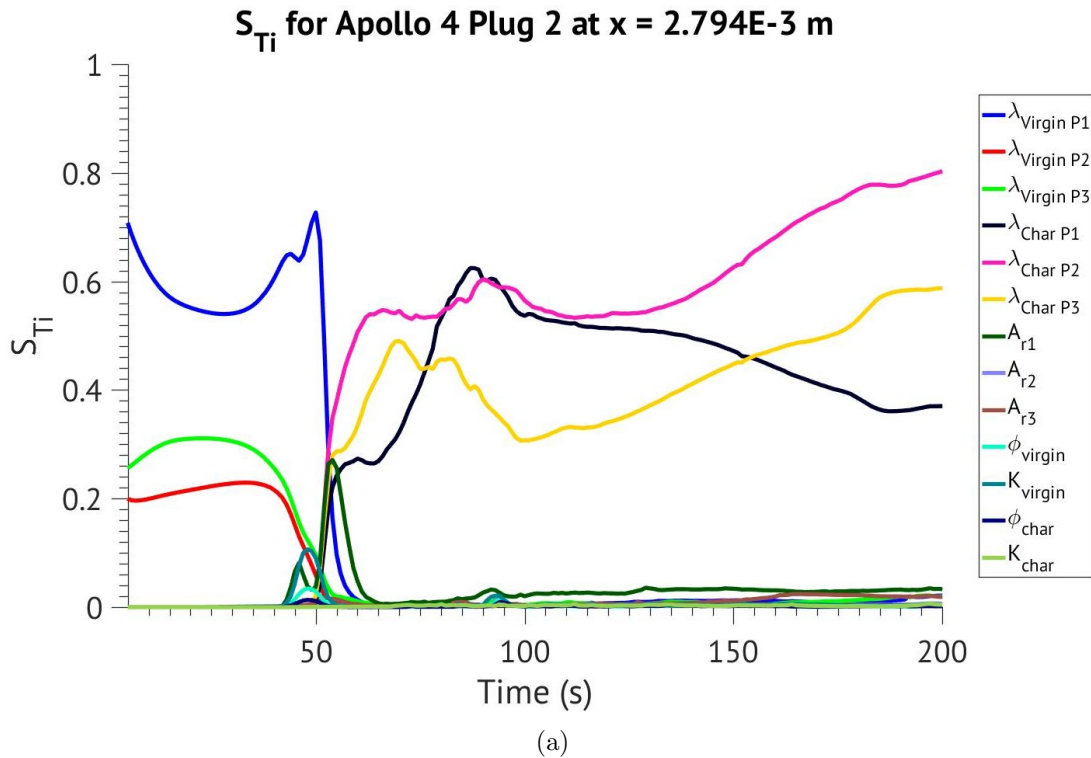


Figure 5.3: Results of the sensitivity study of VISTA performed with the method of Sobol for thermocouples located in Plug 2 of Apollo 4 flight.

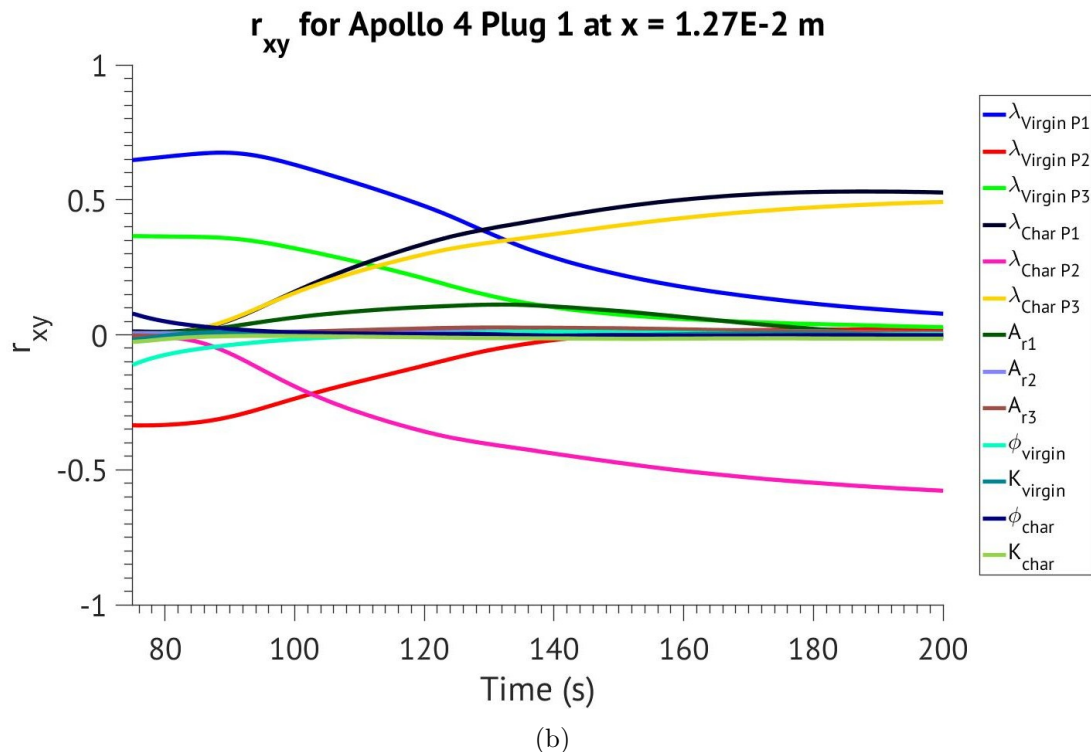
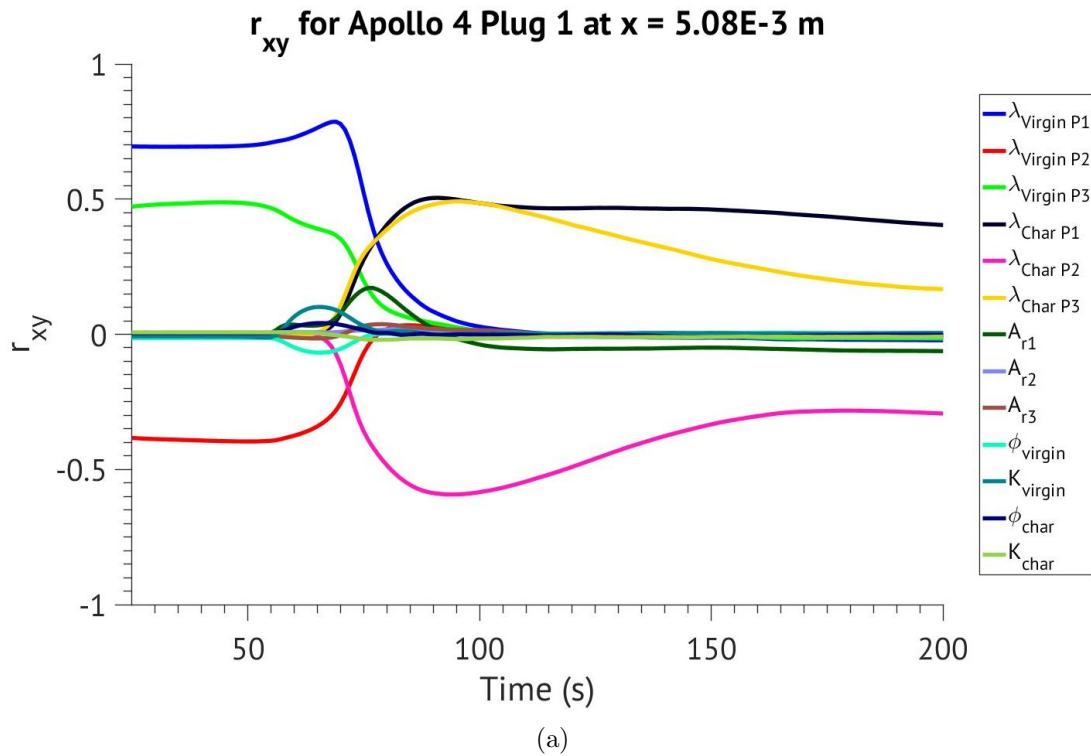


Figure 5.4: Results of the sensitivity study of VISTA in the form of PCCs for thermocouples located in Plug 1 of Apollo 4 flight.

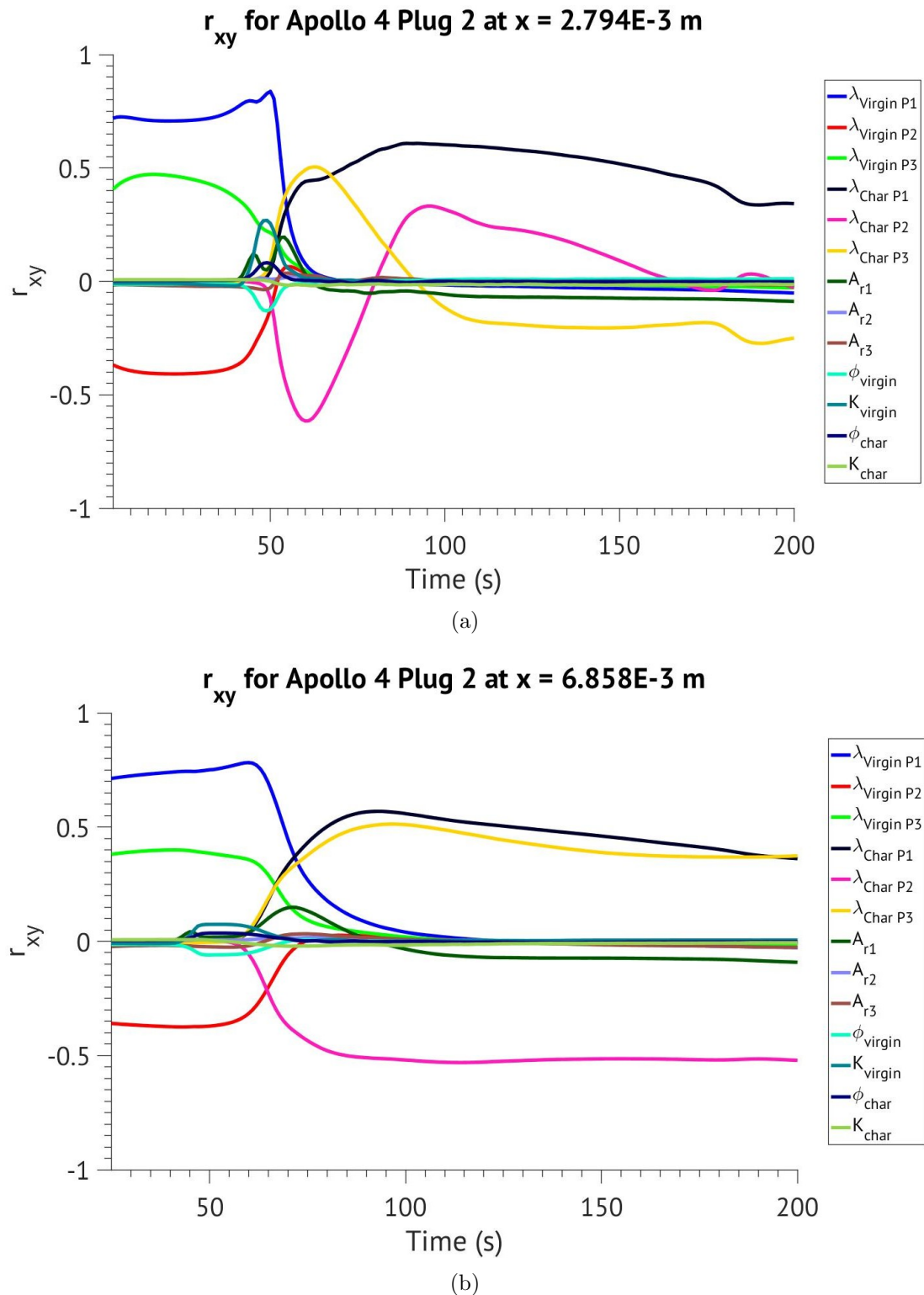


Figure 5.5: Results of the sensitivity study of VISTA in the form of PCCs for thermocouples located in Plug 2 of Apollo 4 flight.

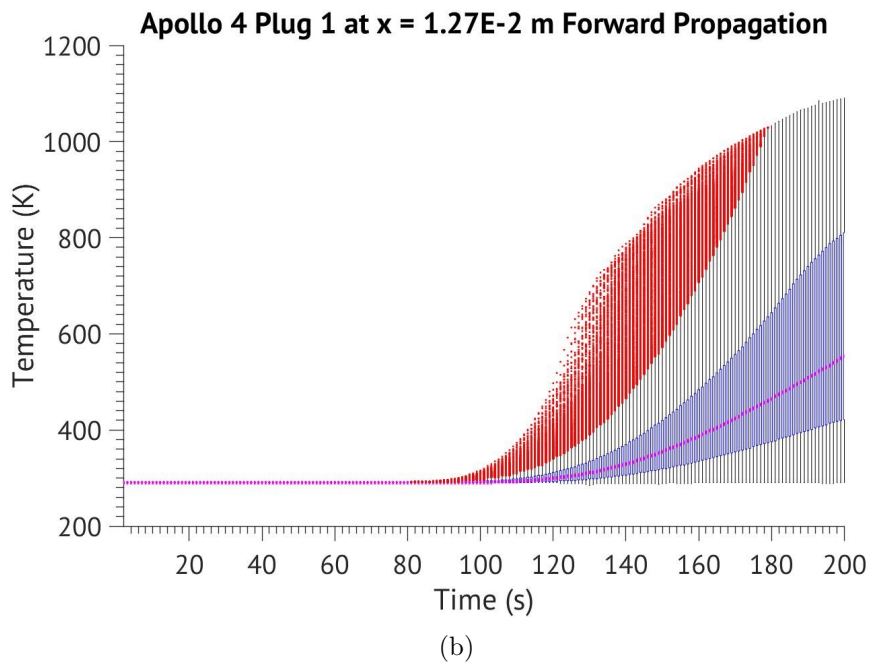
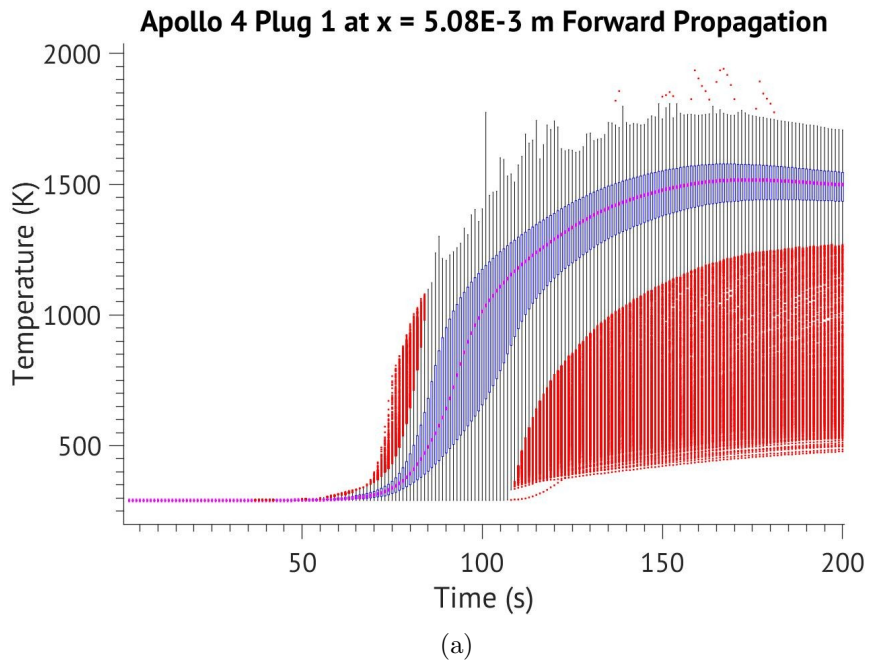


Figure 5.6: Box plots of model outputs resulting from the forward propagation of prior PDFs through the statistical forward problem for Plug 1 where blue lines represent individual boxes limited by the first and third quartiles, black lines are box plot whiskers which extend to minimum and maximum ranges, red dot markers signify the outliers, and magenta lines show the median.

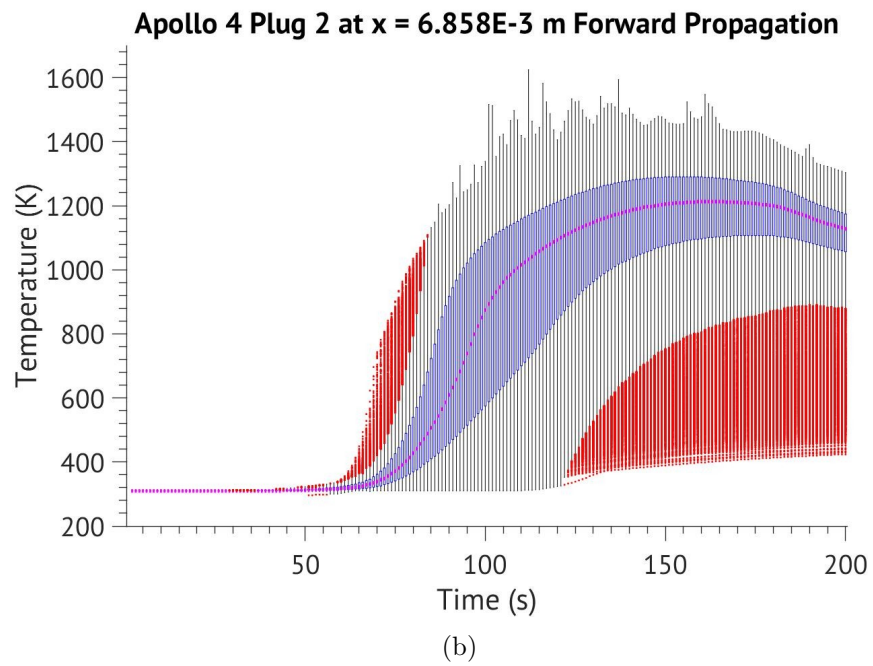
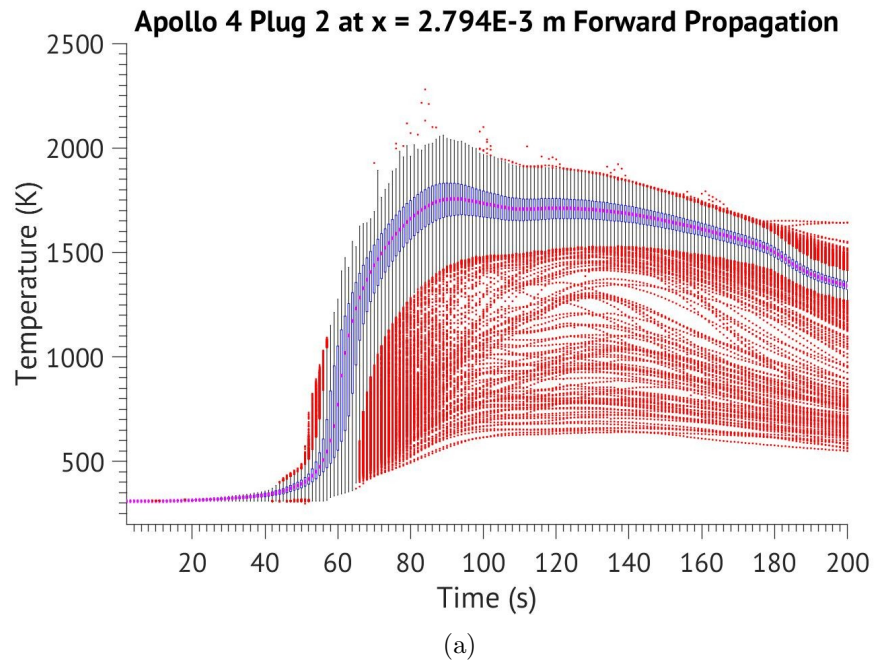


Figure 5.7: Box plots of model outputs resulting from the forward propagation of prior PDFs through the statistical forward problem for Plug 2 where blue lines represent individual boxes limited by the first and third quartiles, black lines are box plot whiskers which extend to minimum and maximum ranges, red dot markers signify the outliers, and magenta lines show the median.

5.2.2 Outcome Discussion

Results of the sensitivity study at each data thermocouple location in each plug are shown in Figures 5.2 and 5.3 for the method of Sobol and Figures 5.4 and 5.5 for Pearson correlation coefficients. The results for the forward propagation of input distributions in Table 5.1 are shown in Figures 5.6 and 5.7 where box plots were graphed in 1s intervals of the time domain respectively for Plugs 1 and 2. In the figures the black line whiskers are set to signify 99.3% confidence intervals in the case of a normal distribution with red dot markers representing outliers; blue colored regions are set to have lower and upper bounds corresponding to first and third quartiles respectively. The final output distribution is observed to be highly skewed with large maximum and minimum bounds of recorded temperatures and a large number of outliers across all four thermocouple locations.

Both sets of sensitivity measures show that the influence of each model parameter on the model output varies significantly with time. However, differences between the results of both methods exist that could lead to contrasting conclusions. The PCCs corresponding to the porosity of char (ϕ_{virgin}) and virgin (ϕ_{virgin}) states imply a non-negligible effect over model output, but method of Sobol casts these two parameters as definitively non-influential. PCCs also show the pre-exponential of the first solid reaction A_{r1} to have significant influence in plot (a) of Figure 5.4 and (b) of Figure 5.5 beyond the 100 second mark whereas that importance is nearly non-existent in the results derived with the method of Sobol. Parameters $\lambda_{char\ P2}$ and $\lambda_{char\ P3}$ are also observed to cross the y-axis in (a) of Figure 5.5 signifying that the linear relationship between parameter and output changes sign. This occurrence also implies that output and stated parameters are not correlated during the time interval enclosing the crossing point. However, same parameters are shown to retain their importance during the corresponding interval in (a) of Figure 5.3. The summand of the Sobol indices in Figures 5.2 and 5.3 is above 1 throughout the scenario consequently revealing that there is a significant presence of higher order parameter interaction effects which exert influence over the model output; computation of Pearson correlation coefficients is not able to capture these interactions. These results lead to the conclusion that method of Sobol is the more appropriate measure to use in the sensitivity study of models approximating charring ablator performance.

Based on the results obtained with the method of Sobol, parameters dictating the functional relationship between thermal conductivities and temperature are

overwhelmingly the most influential parameters over model output across all four locations. The first solid reaction pre-exponential is also shown across all thermocouples to be a significant parameter. The permeability of the virgin state shows minor influence on the output in the shallowest thermocouple of the second plug. The remaining parameters are shown to be non-influential, which justifies their removal from further analysis. It is important to point out that Sobol indices corresponding to parameters dictating the functional form of λ_{char} experience an increase shortly after the influence of the parameters describing the functional relationship of λ_{virgin} begins to decrease. The interval of occurrence of both of these effects coincides with the interval where the influence of the first reaction pre-exponential is present; the duration of this interval also depends on the depth in the material. It can be therefore concluded that this time interval coincides with the time interval during which decomposition mechanics heavily affect material temperature predictions. Errors in modeling the solid decomposition and pyrolysis gas phenomena will affect the temperature output over a larger time domain deep within the material than near the surface. The effect also experiences a lagging effect as the time interval on the per plug basis appears to shift in time based on material depth.

5.3 Calibration and Uncertainty Quantification of VISTA

The layout of following sections is as follows. First a calibration of VISTA model parameters is carried out using synthetic, generated data to prove the validity of the approach utilized in this thesis. The results of the statistical forward problem with comparison to synthetic data are also shown. Following, calibration of uncertain and influential parameters is performed using thermocouple data recorded during Apollo 4 flight test. The solution of the forward statistical problem is then shown and compared with original Apollo 4 calibration data.

The current calibration framework that makes use of Bayesian inference as covered in Chapter 3 consists of aspects that are problem dependent and must be determined apriori by the investigator. These aspects consists of problem dependent assumptions concerning the error form, likelihood function formulation, and model parameter prior distributions representing the state of knowledge concerning their respective values. The following sections present the choices made with respect to each in this work.

5.3.1 Likelihood and Error Form

The formulation of the likelihood function is problem specific. All data points in this case are assumed to be spatially and temporally independent, and a multiplicative error is considered of the form shown in Equation 5.2 where D_i and Y_i respectively represent data and corresponding output points while $\epsilon_{i,tot}$ represents the total error measure.

$$D_i = Y_i \times 10^{\epsilon_{i,tot}} \quad (5.2)$$

The likelihood distribution, and therefore the error, is assumed to follow the Gaussian distribution shown in Equation 5.3 where σ is treated as an uncertain parameter to be calibrated. The parameter serves as a penalization factor in the error between output and data, the magnitude of which signifies the magnitude of the uncertainty present due to modeling assumptions and data inaccuracies combined.

$$p(D|\theta, M) = \frac{1}{\sqrt{(2\pi\sigma^2)^{N_d}}} \exp \left[-\frac{1}{2} \sum_{i=1}^{N_d} \left(\frac{\log_{10}(D_i) - \log_{10}(Y_i)}{\sigma} \right)^2 \right] \quad (5.3)$$

In the present case where calibration is performed with multiple thermocouples from 2 separate plugs, the total likelihood is computed as a product of individual likelihoods of the form of Equation 5.3 where each constituent likelihood introduces their own σ parameter to the uncertain parameter space. The error and likelihood forms defined above are used throughout the remainder of this thesis.

5.3.2 Parameter Priors

Full list of uncertain VISTA model parameters to be calibrated using Apollo 4 flight data are listed in Table 5.2. The included parameters were chosen based on the sensitivity analysis results shown in Figures 5.2 and 5.3. There would be no physical justification for the permeability value of the virgin state to be higher than that of the char state, hence the permeability of the char state state is retained as an uncertain parameter in an attempt to avoid this possibility without strictly enforcing it. However, significant knowledge concerning the parameter value is not expected to be gained. The number of sigma parameters considered is the same as the number of thermocouples from which calibration data were extracted. In effect, a parameter indicating the severity of model and data error will

Table 5.2: List of Uncertain Parameters to be Calibrated.

| Input Parameters | Parameter | Sampling Distribution |
|-----------------------------------|--------------------------|-----------------------|
| Virgin State Thermal Conductivity | $\lambda_{virgin\ P1}$ | $U[0.06, 0.15]$ |
| | $\lambda_{virgin\ P2}$ | $U[400, 650]$ |
| | $\lambda_{virgin\ P3}$ | $U[200, 800]$ |
| Char State Thermal Conductivity | $\lambda_{char\ P1}$ | $U[0.8, 1.8]$ |
| | $\lambda_{char\ P2}$ | $U[1500, 2700]$ |
| | $\lambda_{char\ P3}$ | $U[600, 1600]$ |
| First Reaction Pre-Exponential | A_{r1} | $10^{U[7,10]}$ |
| Virgin State Permeability | K_{virgin} | $10^{U[-12,-9]}$ |
| Char State Permeability | K_{char} | $10^{U[-12,-9]}$ |
| Model and Data Error Plug 1 TC1 | $\sigma_{Likelihood\ 1}$ | $U[0, 0.05]$ |
| Model and Data Error Plug 1 TC2 | $\sigma_{Likelihood\ 2}$ | $U[0, 0.05]$ |
| Model and Data Error Plug 2 TC1 | $\sigma_{Likelihood\ 3}$ | $U[0, 0.05]$ |
| Model and Data Error Plug 2 TC2 | $\sigma_{Likelihood\ 4}$ | $U[0, 0.05]$ |

be calibrated at each location in the ablating material where data were recorded.

5.3.3 Calibration with Manufactured Data

Prior to calibration with Apollo 4 flight data, manufactured data is generated with a set of nominal VISTA parameter values for the Apollo 4 scenario. Furthermore, multiplicative noise of the form of Equation 5.2 is added following a Gaussian distribution. Instead of a single 3-D simulation, two independent 1-D simulations are used in tandem to both lower the computational costs of the calibration scenario and more closely replicate practical design process structure of thermal protection systems. However, calibration is still performed with model output from both simulations simultaneously while using same sampled material parameters. Each 1-D simulation corresponds to a plug located on Apollo 4's aft heat shield which uses manufactured temperature data as the TC driver thermal boundary condition. The purpose of this effort is to demonstrate that nominal parameter values can be extracted from the Apollo 4 scenario.

Posterior PDFs for the selected VISTA model parameters are shown in Figure 5.8 where dashed lines indicate nominal parameter values with which data were generated. The results were obtained using only 5 chains and a total of 22,000 accepted samples with a burn in of 2,000 samples per chain. It is observed that nominal functional relationships between the thermal conductivity of virgin and char states and temperature are retrieved. The posterior PDF of the thermal

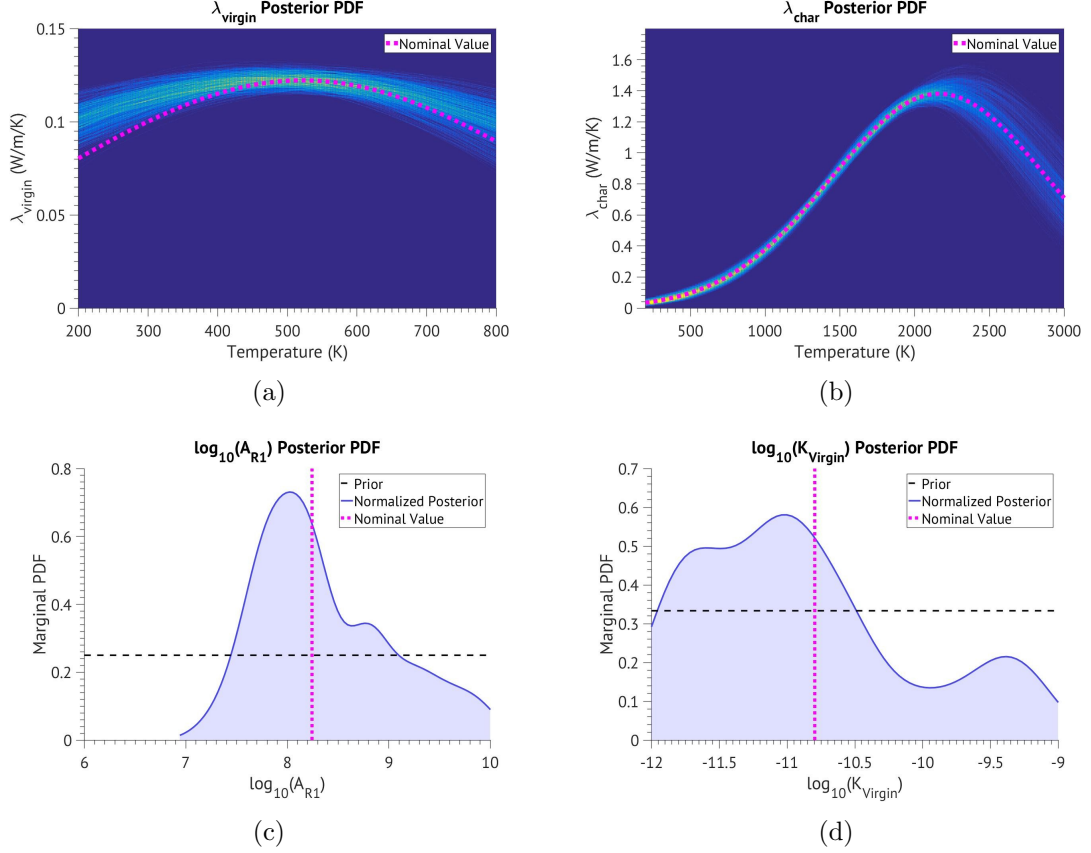


Figure 5.8: Posterior PDFs of selected VISTA model parameters obtained through the solution of the statistical inverse problem using manufactured data.

conductivity of the char state λ_{char} shows the highest confidence in the results, agreeing with the conclusion drawn from the sensitivity analysis that it was the most influential parameter being considered. The high uncertainty in the values past the temperature of 2200K is due to significant amount of material in the manufactured case never reaching temperatures that high; very little information about the parameter behavior in that temperature range could be extracted from model output. Same argument is invoked for the reason why the calibrated result corresponding to the thermal conductivity of the virgin state λ_{virgin} below the temperature of 300K shows slight deviation from nominal values; the material temperature in the scenario across all four locations never fell below approximately 290K and experienced very low variation in the 290 – 350K range across most thermocouples. The calibrated relationship between λ_{virgin} and temperature though still shows good agreement with the nominal trend. Smaller confidence in its functional form reflects the fact that the influence of the parameter is sig-

nificant in the portion of the simulation that experienced small variations in the output. Even though two of the constituent parameters were shown to exhibit limited influence over the output in the sampled range, the nominal functional relationship was approximately retrieved. The posterior of the first solid reaction rate A_{r1} shows a moderate certainty in the most probable value obtained. Based on the sensitivity analysis results, the wide posterior PDF is due to the parameter showing minor influence on the output in the manufactured data scenario. However, the most probable value aligns well with the nominal value used and uncertainty would be expected to decrease with a larger number of samples. The posterior PDF corresponding to the permeability of the virgin state K_{virgin} shows the most probable value being extremely close to the nominal result. However, the PDF also shows large uncertainty reflecting the fact that it showed very low influence on the output. This can also be due to the fact that significant noise was added to data. Permeability of the char state K_{char} parameter never exhibited convergent behavior as it was a non-influential parameter that was included only as a sanity check, therefore it was excluded from Figure 5.8.

The statistical forward problem was also solved for the manufactured data case. The solution is shown in Figures 5.9 and 5.10; data generated before and after noise was added are included in the figures. The resulting posterior distributions are approximately Gaussian allowing for 3σ (99.7%) confidence intervals to be constructed. The most probable deterministic outputs are observed to be in almost perfect agreement with nominal outputs across all figures showing that the calibration is accurate even though significant noise to data was added. This conclusion is reinforced by looking at Figures 5.11 and 5.12 where the β HPD values based on nominal model output are near unity. All data with noise applied are also completely encapsulated by the drawn CIs.

Based on these results, the methodology employed in this work is proven to be able to calibrate influential VISTA model parameters in ablation scenarios by being able to retrieve nominal parameter values and final deterministic outputs across all four thermocouple locations in the manufactured case. It is also anticipated that knowledge of parameter values will be improved upon the most for parameters that showed significant influence on the output within time intervals that experienced highest variance during the sensitivity study.

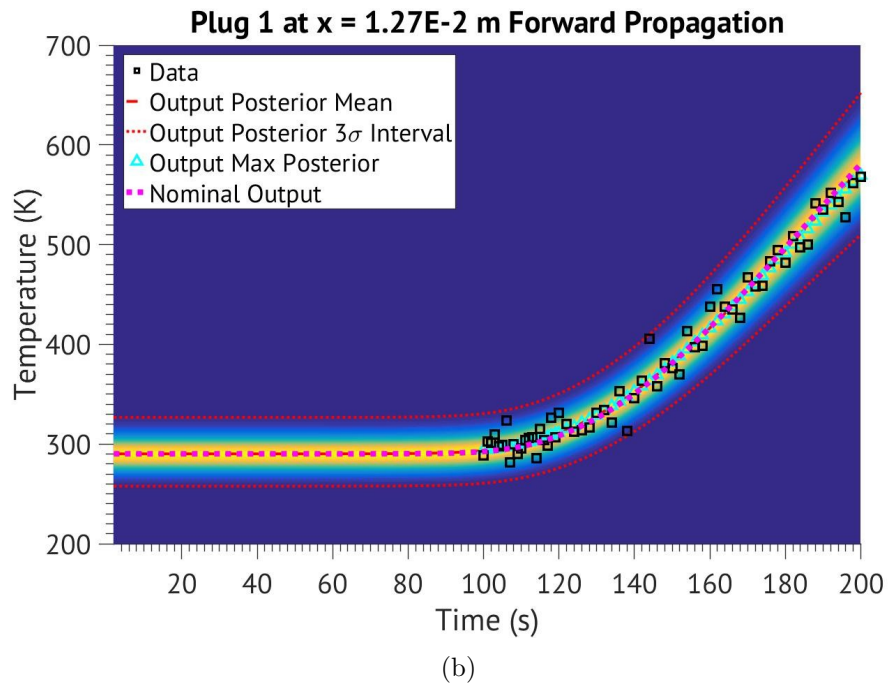
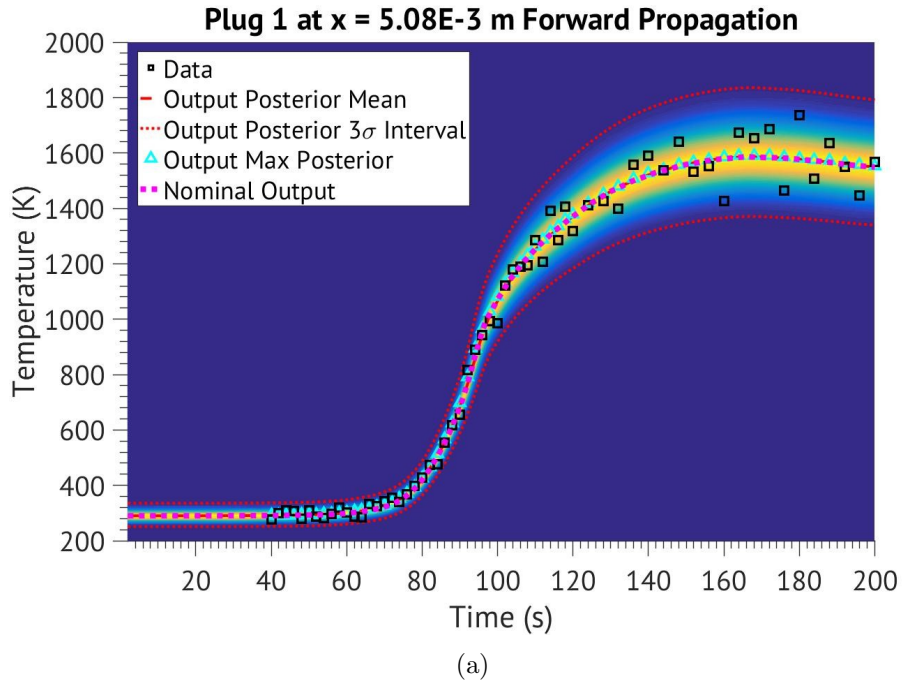


Figure 5.9: Solution plots of the forward propagation of calibrated VISTA parameter PDFs through the statistical forward problem for thermocouple locations in Plug 1 of the manufactured case.

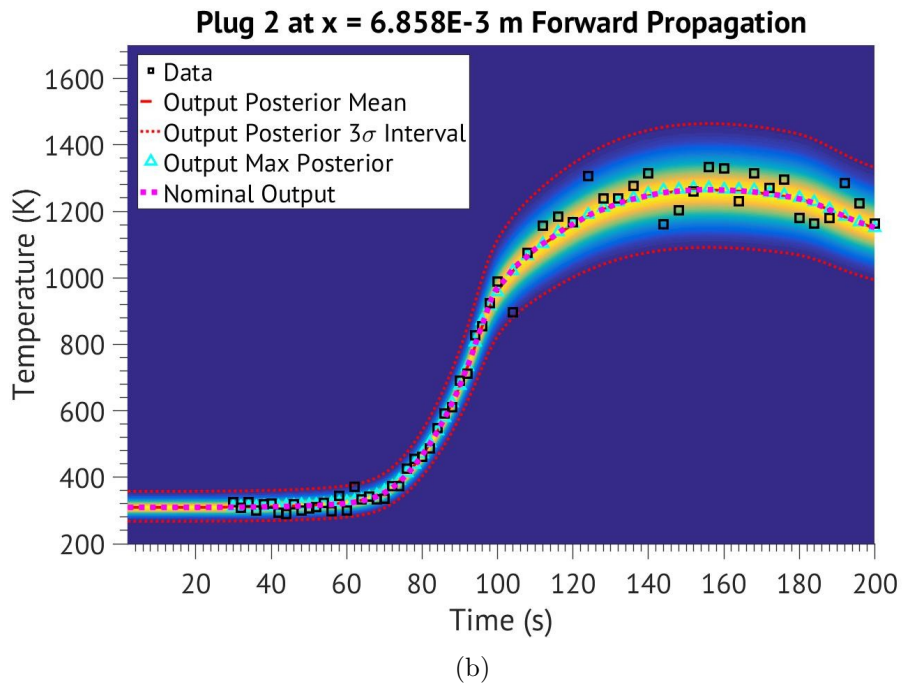
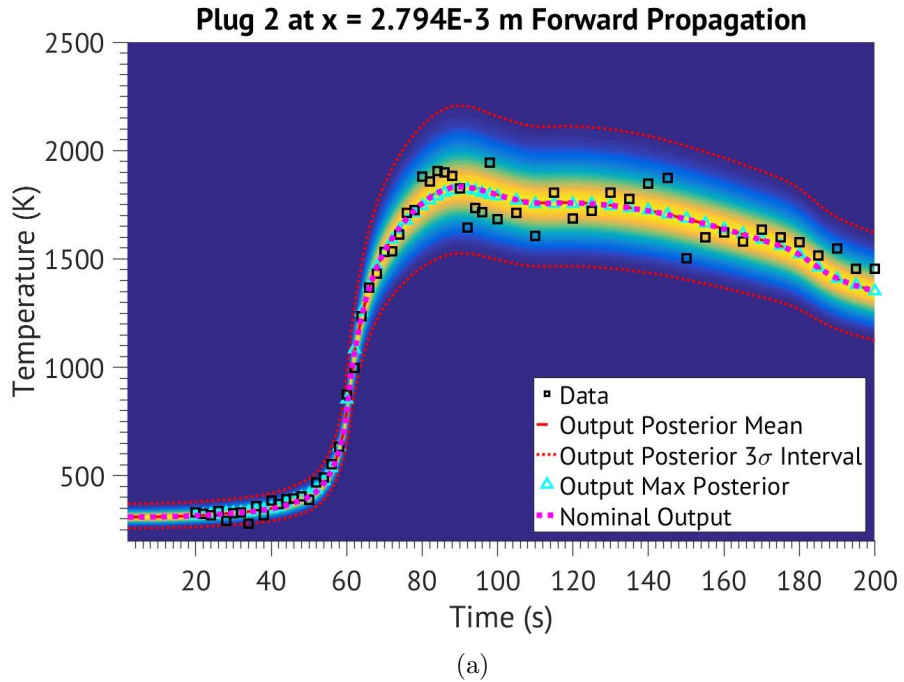


Figure 5.10: Solution plots of the forward propagation of calibrated VISTA parameter PDFs through the statistical forward problem for thermocouple locations in Plug 2 of the manufactured case.

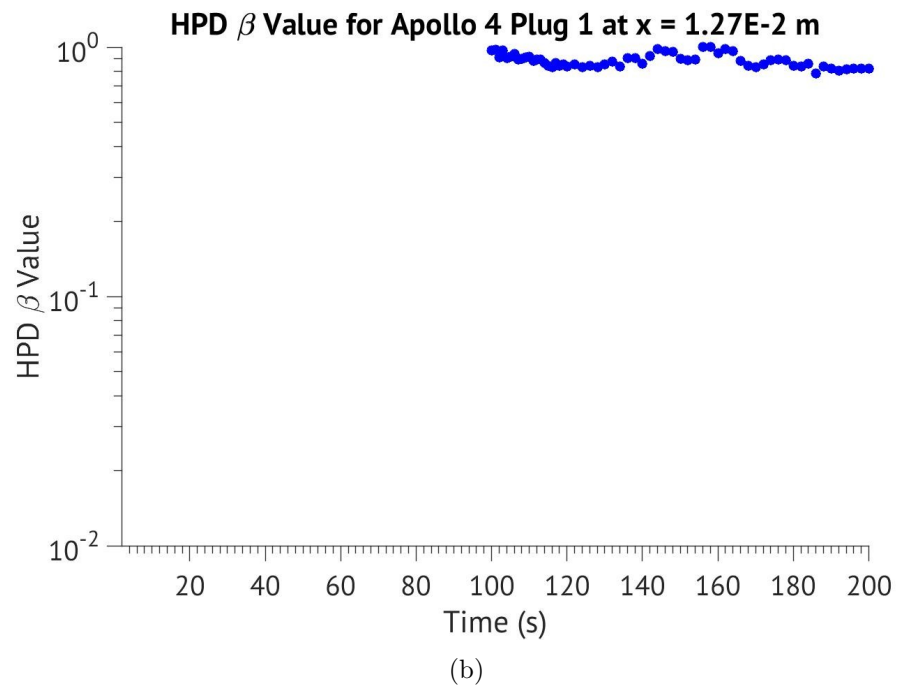
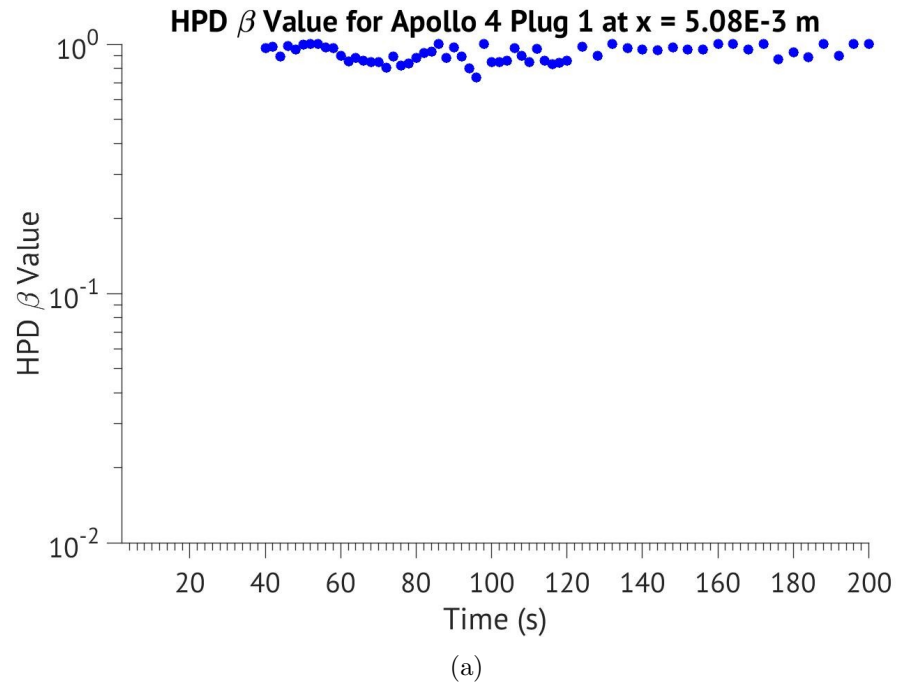


Figure 5.11: HPD β values derived using nominal model output values for likelihood nodes at thermocouple locations in Plug 1 of the manufactured data case.

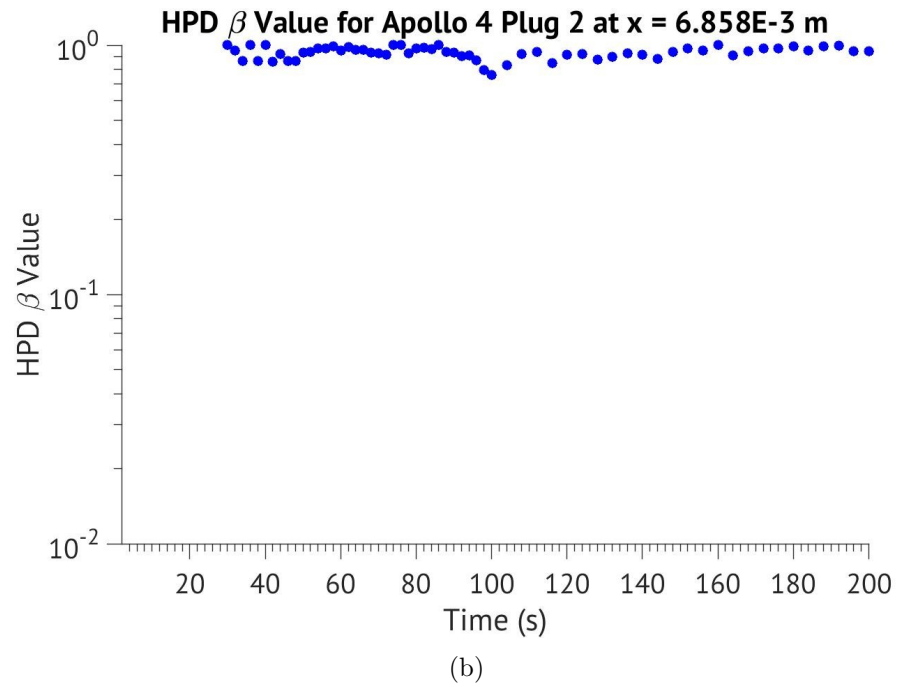
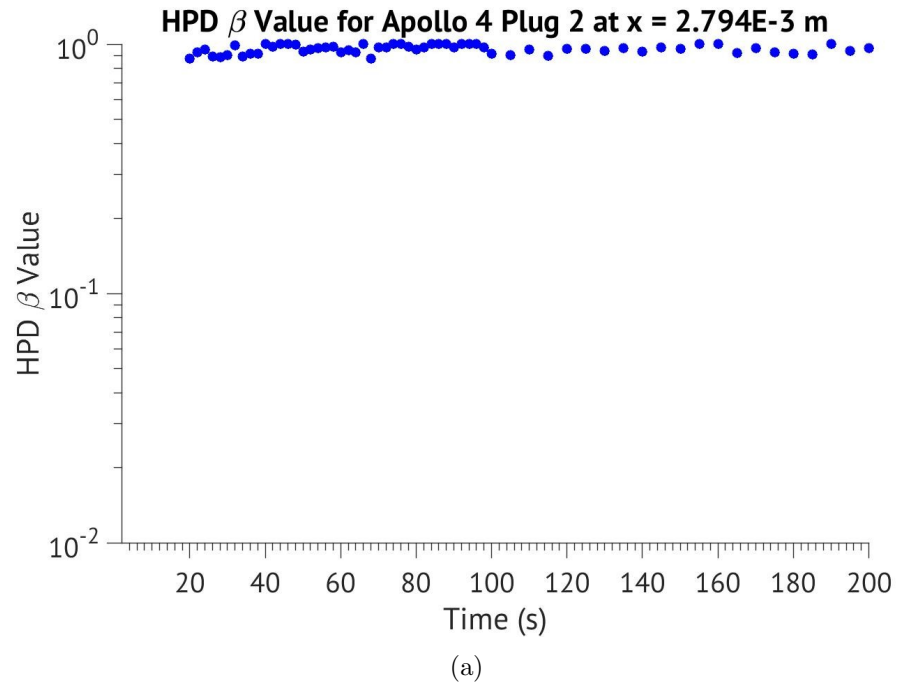


Figure 5.12: HPD β values derived using nominal model output values for likelihood nodes at thermocouple locations in Plug 2 of the manufactured data case.

5.3.4 Calibration with Flight Data

In the calibration of VISTA using Apollo 4 flight data, all indicated parameters in Table 5.1 are considered as uncertain. The calibration data in this scenario consists of material temperature profile history collected with two sets of two thermocouples across two plugs at different material depths shown in Figure 5.1. Each 1-D simulation again corresponds to a plug located on Apollo 4's aft heat shield and uses Apollo 4 flight temperature recordings of the thermocouple nearest to the surface as the TC driver thermal boundary condition; a σ parameter is again considered per each thermocouple data source.

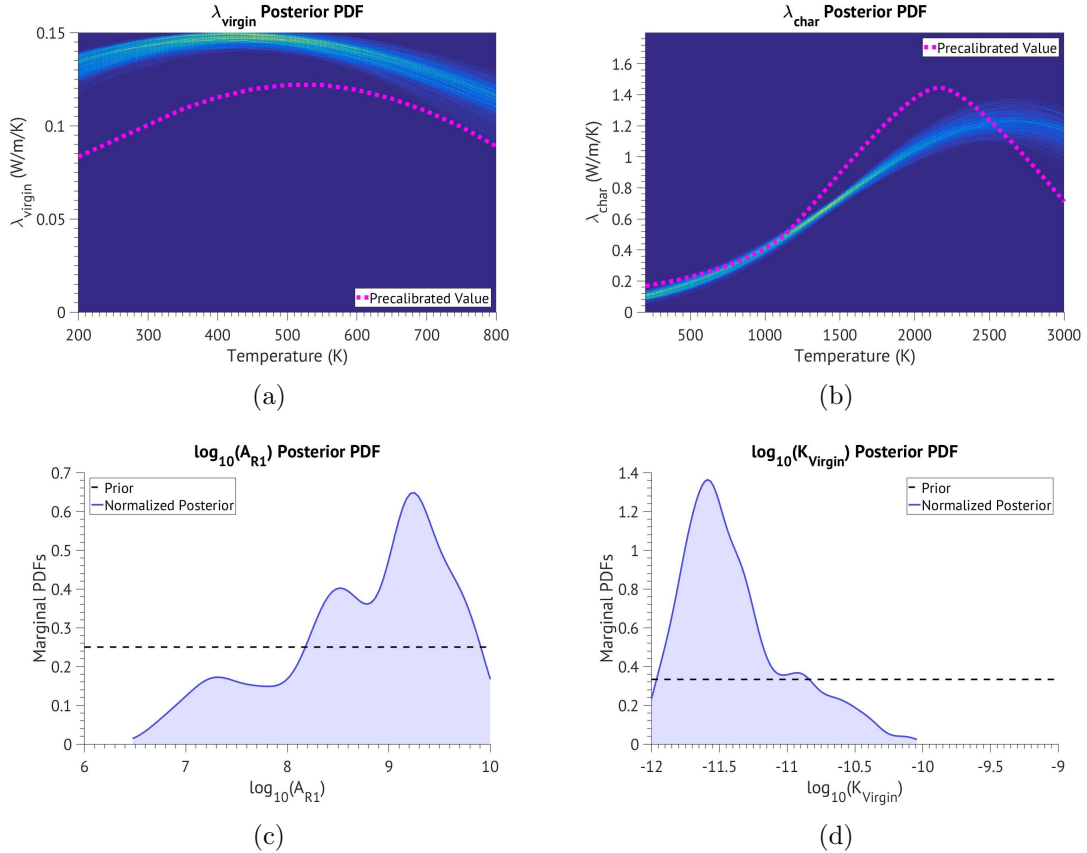


Figure 5.13: Posterior PDFs of sensitive VISTA model parameters obtained through calibration with Apollo 4 flight data.

Posterior PDFs corresponding to sensitive and uncertain VISTA model parameters obtained through the solution of the statistical inverse problem are shown in Figure 5.13 where significant departures from pre-calibrated values are observed across the entire parameter space. In the case of the λ_{virgin} , the calibrated functional relationship has its peak value occur with a larger magnitude at smaller

temperatures. The range of the prior for λ_{virgin} functional relationship was in fact observed to prevent larger values of the thermal conductivity from being explored; numerous samples failed due to $\lambda_{virgin} P_1$ falling outside the defined prior range. This is believed to have caused other less sensitive parameters that sampled well within their bounds from having narrow posterior PDFs and exhibit slight multi-modal behaviors. In future calibration efforts, the ranges of the priors of the parameters defining the relationship between λ_{virgin} and temperature must be extended. The priors of parameters that define the function of λ_{char} on the other hand were satisfactory and the solution shows a well defined and narrow posterior PDF throughout most of the temperature domain. Above the temperature of 2500K, the amount of uncertainty in the results increases due to significant portions of the material again never reaching temperatures of that magnitude. Therefore, it is difficult to extract more information about parameter behavior past the temperature of 2500K. The results show that between the temperatures of approximately 1200K and 2500K, the calibrated λ_{char} values are lower in magnitude than previously believed. At lower temperature ranges the pre-calibrated values of λ_{char} are nearly the same as the calibrated result. The first reaction pre-exponential A_{r1} parameter posterior PDF shows that a value of almost a magnitude larger than original is most probable. The posterior distribution for the permeability of the virgin state K_{virgin} also shows a large gain in the information about the parameter with the most probable value being half of the original. As such, updated knowledge of the the material after calibration dictates a lower tendency to develop fluid flow through it in its virgin state. The large reduction in uncertainty from prior distributions means that Apollo 4 data contained enough information about these parameters for their calibration. On the other hand, the posterior PDF for the permeability of the char state never converged and spans the entire domain of the prior in a nearly uniform manner just as the sensitivity study suggested would occur; the result is hence not included in the results presented. The results of the calibration with pre-calibration and most probable post-calibration values can be found in Table 5.3 for non-tabulated parameters and Figure 5.14 for the thermal conductivity of virgin and char states.

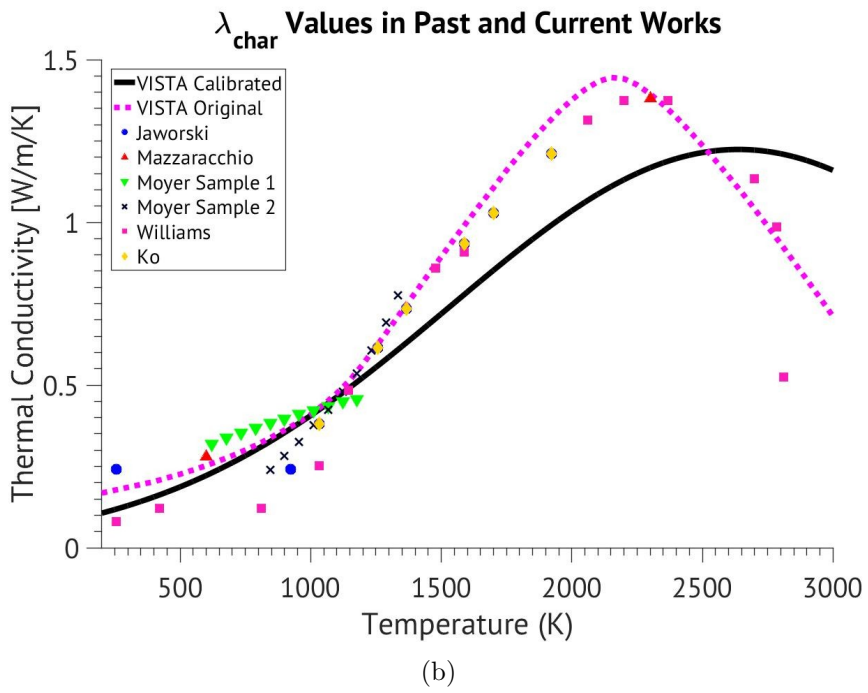
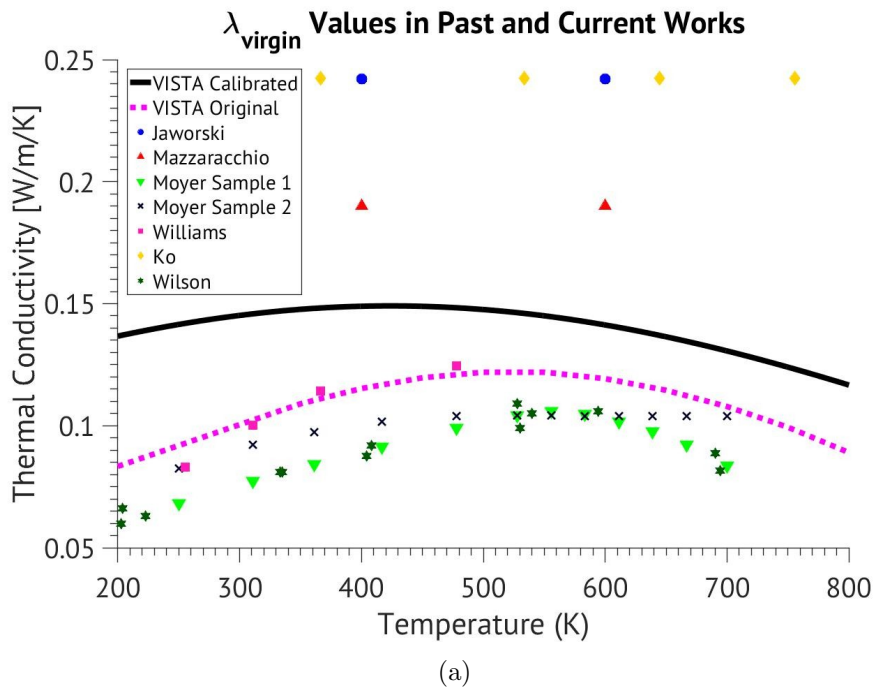


Figure 5.14: Comparison of virgin (a) and char (b) state thermal conductivity values found in other works with calibration results of the present study [14].

Table 5.3: Most Probable Calibrated Values of Non-tabulated Parameters.

| Model Parameters | Original Value | M. P. Calibrated Value |
|--------------------------------|-----------------------|--------------------------|
| First Reaction Pre-Exponential | 1.75×10^8 | 1.7865×10^9 |
| Virgin State Permeability | 1.6×10^{-11} | 2.5704×10^{-12} |
| Char State Permeability | 2.0×10^{-11} | N/A (Insensitive) |

5.3.5 Uncertainty Quantification

To observe the effect of the calibration process using Bayesian inference on the final output, the posterior model parameter PDFs as well as model and data error parameters were forward propagated through the statistical forward problem using the same scenario case. The results of the exercise are shown in Figures 5.15 and 5.16 for all four thermocouples from which calibration data were extracted. In addition, pre-calibration output as well as material temperature data are plotted for comparison.

Improvements across temperature outputs at all locations are observed. The maximum posterior probability outputs align closer with observed data than output generated with pre-calibration model parameter values for majority of the time domain across all figures. Largest relative gains can be observed at the deepest thermocouple locations in Plugs 1 and 2. The most probable calibrated outputs, however, do not identically replicate flight data. Output posterior distributions at all locations are approximately Gaussian which allows for the computation of 99.7% confidence intervals. Different CIs per each location are observed due to the calibration of a σ model and data error parameter per each data source. The solution of the statistical inverse problem consisted of differing posterior PDFs of these parameters that were in this case dependent on the thermocouple location in the Apollo 4's aft heat shield. The CI is seen to be the smallest at the location of the deepest thermocouple in Plug 1 shown in (b) of Figure 5.15 while the largest magnitude of uncertainty in the output is observed at the shallowest thermocouple location in (a) of the same figure. Same pattern can be observed in Figure 5.16 where output uncertainty within the same plug was observed to be greatest near the origin. Based on the values of the β parameters of HPD intervals plotted in Figures 5.17 and 5.18, the calibrated model has difficulties replicating calibration data during certain time intervals. These intervals are however short and the value of β never takes on values below 0.01 which the authors of Ref. [19] recognized as an acceptable threshold value below which a data point becomes an

improbable outcome of the model. Beyond these intervals the model in general performs well with respect to data across all locations based on β HPD plots.

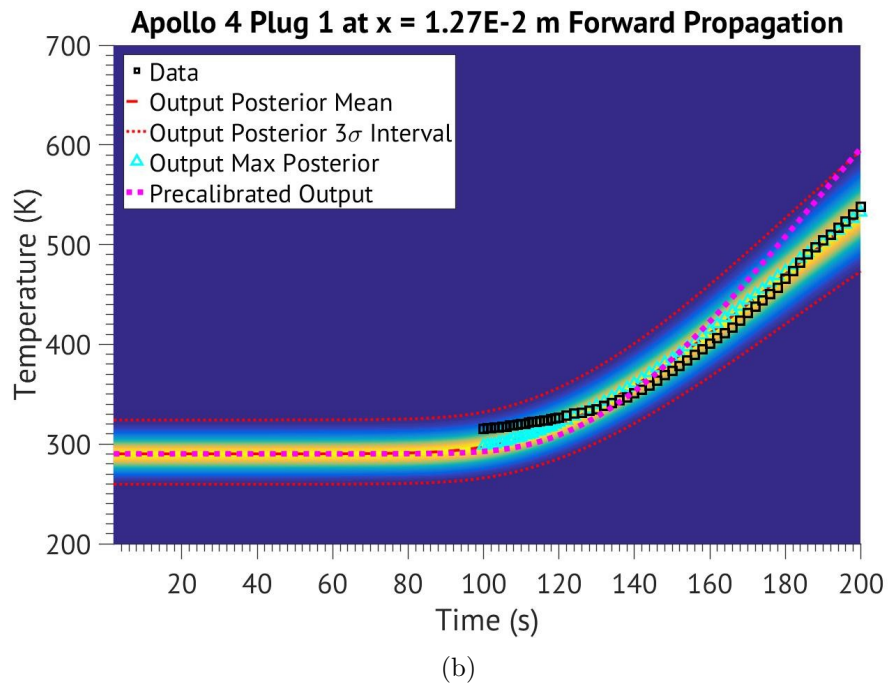
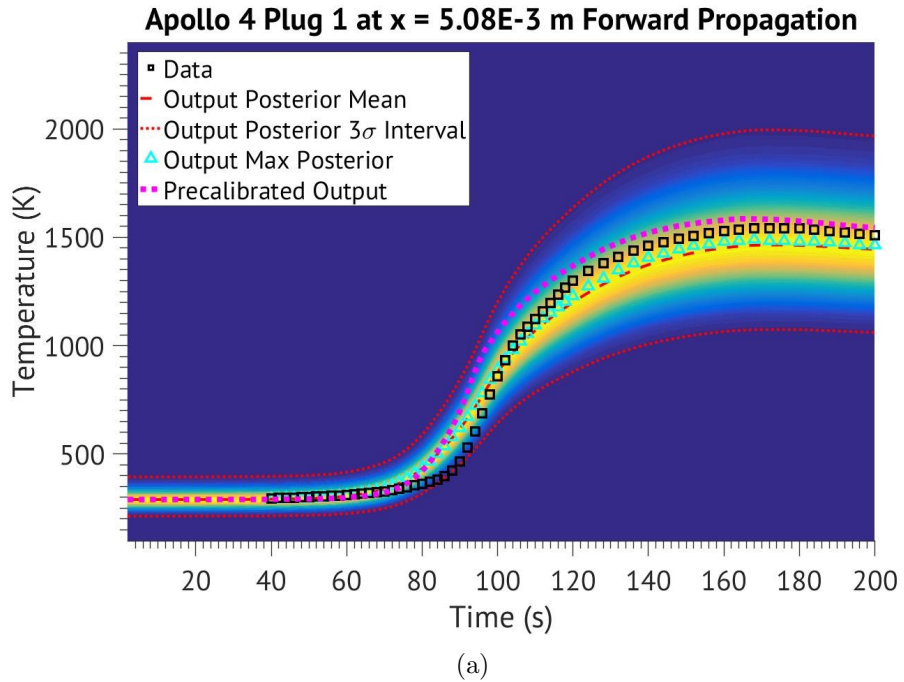


Figure 5.15: Solution plots of the forward propagation of calibrated VISTA parameter PDFs through the statistical forward problem for thermocouple locations in Plug 1 of the Apollo 4 scenario.

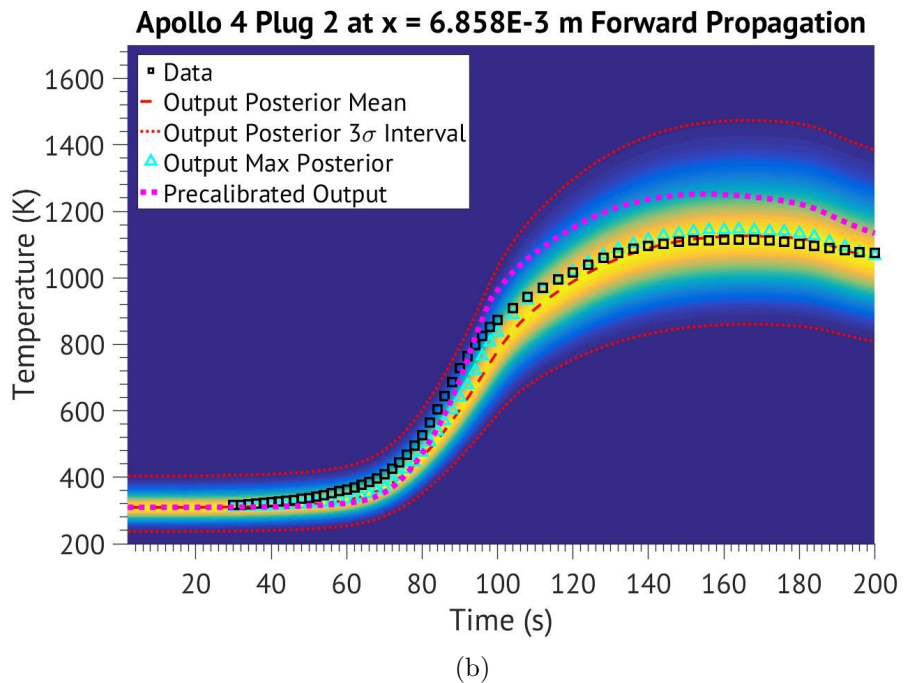
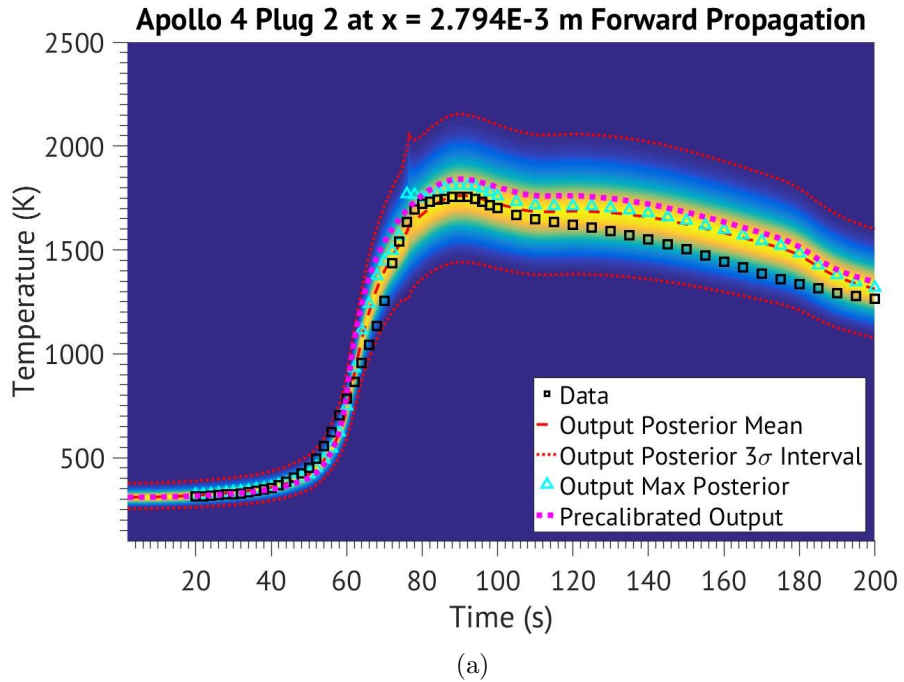


Figure 5.16: Solution plots of the forward propagation of calibrated VISTA parameter PDFs through the statistical forward problem for thermocouple locations in Plug 2 of the Apollo 4 scenario.

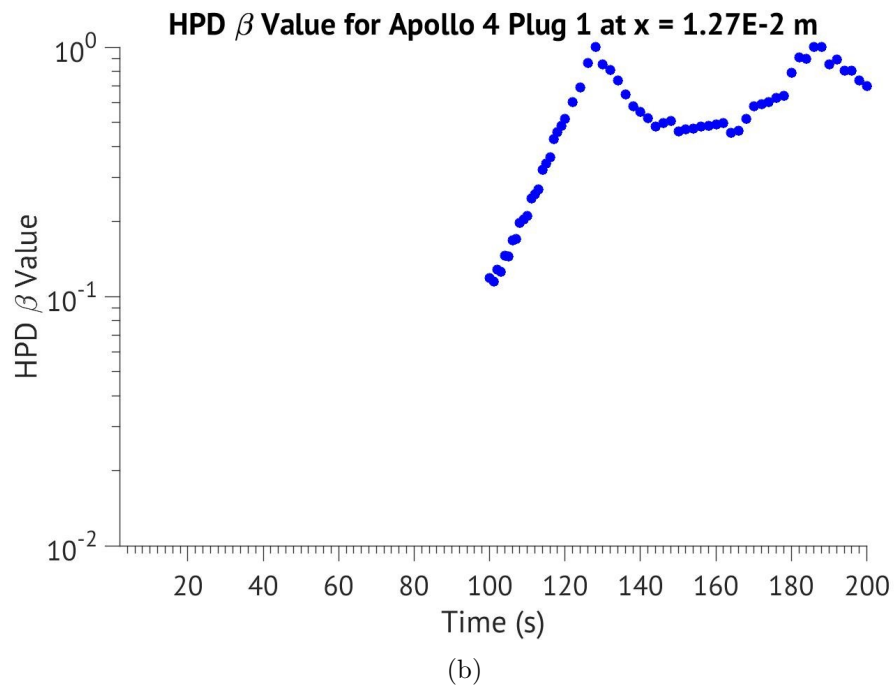
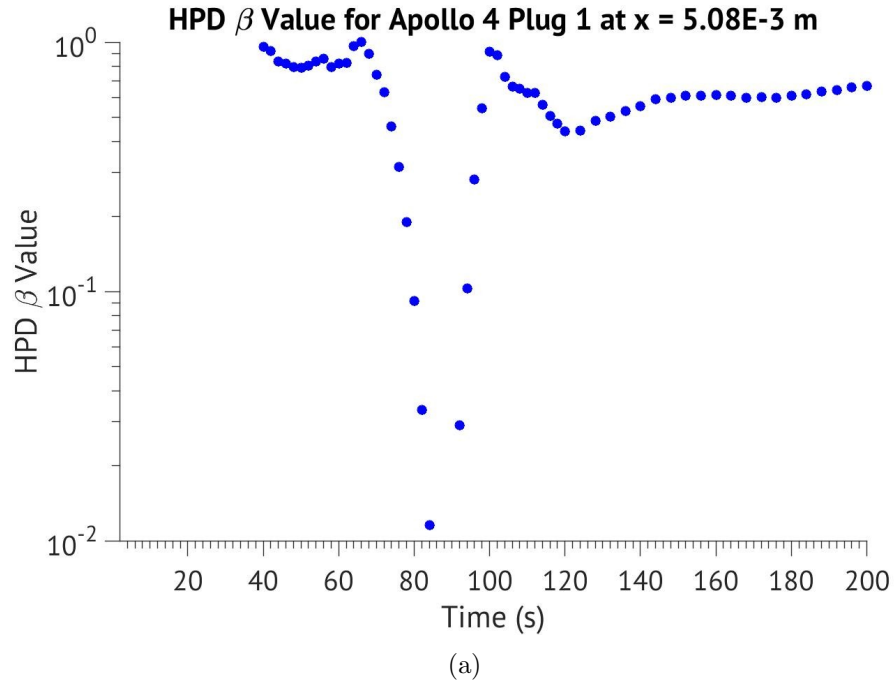


Figure 5.17: HPD β values derived for likelihood nodes at thermocouple locations in Plug 1 of the Apollo 4 scenario.

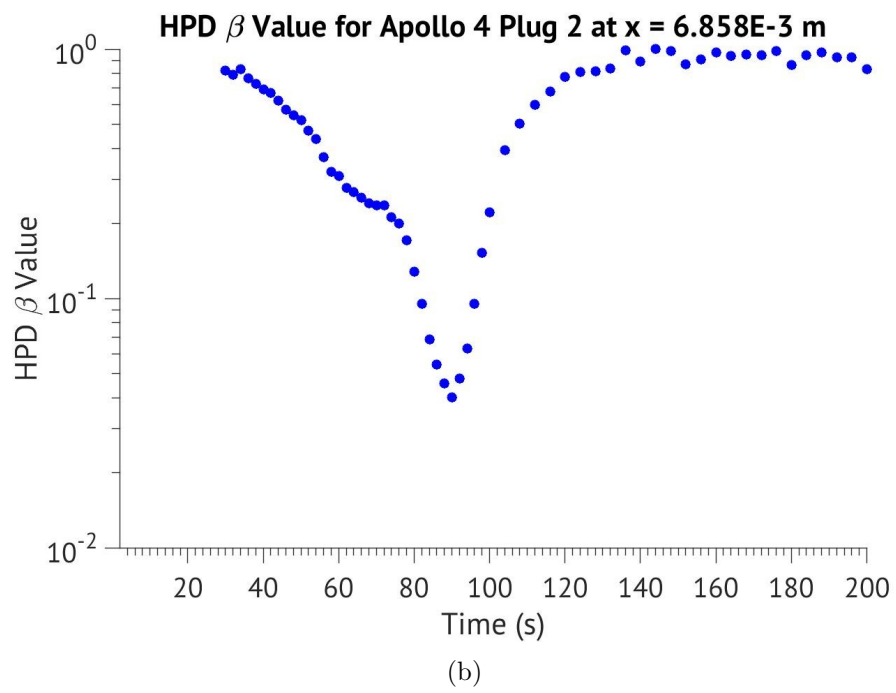
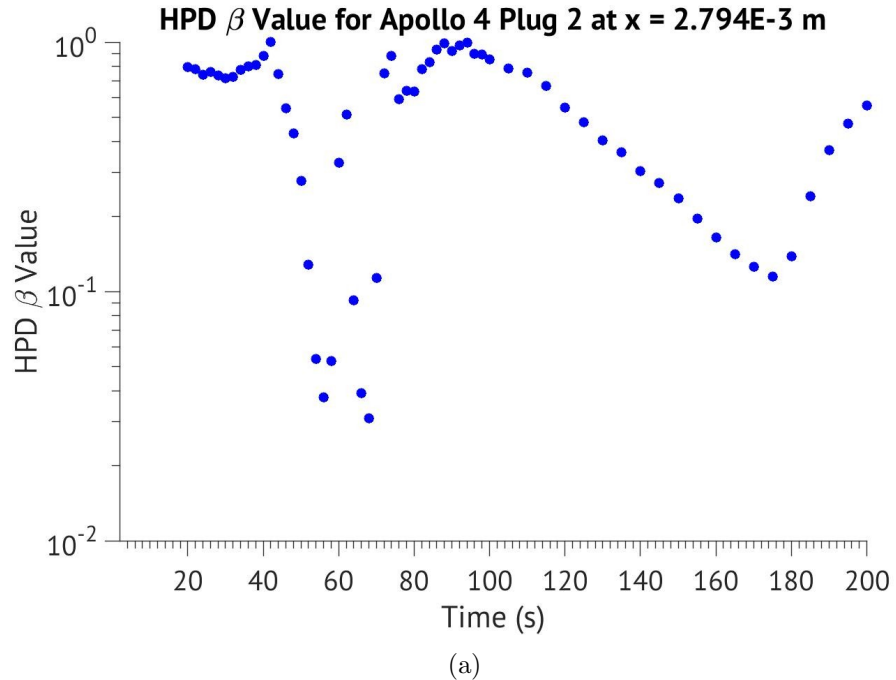


Figure 5.18: HPD β values derived for likelihood nodes at thermocouple locations in Plug 2 of the Apollo 4 scenario.

Chapter 6

Conclusions

In this thesis a sensitivity analysis study was performed on the open-source AV-COAT similar VISTA material database. Following, calibration of the uncertain VISTA parameters was undertaken through the use of Bayesian inference combined with material temperature data collected during the Apollo 4 flight. Uncertainties due to parameter, model, and data errors were then forward propagated onto the output. The methodology employed here took full advantage of being able to express knowledge of a system in terms of probability distribution functions. In turn, calibration through a Bayesian approach allowed for the state of knowledge prior PDFs defined for each parameter to be updated based on newly acquired data. The calibration process also quantified the uncertainty present in model output due to model structure errors and uncertainty present in the readings provided by recording hardware and possibly data post-processing software. Ability to account for uncertainties caused by all three stated sources and expression of model output in terms of a PDF enables engineers to implement safety factors that are based on the computed uncertainty bounds instead of past designs and subjective opinions; the methodology is also likely to cause smaller safety factors to be implemented into final products.

The benefits of the employed method are evident in the reduction of uncertainty achieved in the model output. When compared to the uncertainty quantification results obtained using the state of knowledge of the system prior to calibration effort, forward propagation of calibrated parameter probability distributions resulted in an output PDF that exhibited much smaller magnitude of uncertainty. This uncertainty included contributions due to parametric, model inadequacy, and data inaccuracy sources that were obtained in a rigorous manner instead of depending on subjective assumptions. In addition, the most probable calibrated deterministic output aligned closer with calibration data supplied for the calibration exercise.

Finally, the approach outlined in this work as well as its implementation in

SMUQ is not model specific and consequently can be utilized with models encountered in many branches of science. In the future, calibration and uncertainty quantification through the use of Bayesian inference will be enhanced due to a planned implementation of surrogate modeling techniques, such as the generalized Polynomial Chaos expansions, aimed at reducing the computational expense of the method that is associated with complex models.

References

- [1] “Nasa strategic plan 2014,” 2014, NASA, Washington, DC.
- [2] “Atmospheric re-entry demonstrator,” 2002, ESA. [Online]. Available: <https://mars.jpl.nasa.gov/mer/gallery/artwork/hires/entry.jpg>
- [3] J. D. Anderson, *Hypersonic and High-Temperature Gas Dynamics, Second Edition*. Reston, VA: AIAA, 2006.
- [4] D. Bose, M. Olson, B. Laub, T. White, J. Feldman, J. Santos, S. Lobo, M. Mahzari, M. MacLean, and A. Dufrene, “Initial assessment of mars science laboratory heatshield instrumentation and flight data,” in *51st AIAA Aerospace Sciences Meeting*. Grapevine, TX: AIAA 2013-908, January 2013.
- [5] A. Martin and I. Boyd, “Modeling of heat transfer attenuation by ablative gases during the stardust re-entry,” in *50th AIAA Aerospace Sciences Meeting*. Nashville, TN: AIAA 2012-0814, June 2012.
- [6] H. K. Tran, C. E. Johnson, D. J. Rasky, F. C. L. Hui, M. Hsu, T. Chen, Y. K. Chen, D. Paragas, and L. K, “Phenolic impregnated carbon ablators (pica) as thermal protection systems for discovery missions,” Moffett Field, CA, NASA 110440, 1997.
- [7] J. E. Pavlosky and L. G. Leger, “Apollo experience report- thermal protection subsystem,” Houston, TX, NASA TN D-7594, 1974.
- [8] H. Weng, “Multidimensional modeling of pyrolysis gas transport inside orthotropic charring ablators,” Ph.D. dissertation, University of Kentucky, Lexington, KY, Dec. 2014.
- [9] “Stardust entry capsule with pica heatshield at end of mission,” NASA, Washington, DC. [Online]. Available: <https://www.nasa.gov/sites/default/files/capsule.jpg>
- [10] C. Johnston, P. Gnoffo, and A. Mazaheri, “Study of ablation-flowfield coupling relevant to the orion heatshield,” *Journal of Thermophysics and Heat Transfer*, vol. 26, no. 2, pp. 213–221, 2012.

- [11] Y. K. Chen and F. S. Milos, “Ablation and thermal response program for spacecraft heatshield analysis,” *Journal of Spacecraft and Rockets*, vol. 36, no. 3, pp. 475–483, 1999.
- [12] M. Stackpole, S. Sepka, I. Cozmuta, and D. Kontinos, “Post-flight evaluation of stardust sample return capsule forebody heatshield material,” in *46th AIAA Aerospace Sciences Meeting and Exhibit*. Reno, NV: AIAA 2008-1202, January 2008.
- [13] D. Bose, T. White, M. Mahzari, and K. Edquist, “Reconstruction of aerothermal environment and heat shield response of mars science laboratory,” *Journal of Spacecraft and Rockets*, vol. 51, no. 4, pp. 1174–1184, 2014.
- [14] A. Omidy, J. M. Cooper, R. Fu, H. Weng, and A. Martin, “Development of an open-source avcoat material database, vista,” in *47th AIAA Thermophysics Conference*. Denver, CO: AIAA Paper 2017-3356, June 2017.
- [15] D. M. Curry and E. W. Stephens, “Apollo ablator thermal performance at superorbital entry velocities,” NASA, Tech. Rep. TN D-5969, Sep. 1970.
- [16] A. Tarantola, *Inverse Problem Theory and Methods for Model Parameter Estimation*. Philadelphia, PA: SIAM, 2005.
- [17] D. S. Sivia and J. Skilling, *Data Analysis: A Bayesian Tutorial*. Chichester, West Sussex, England: Oxford University Press, 2006.
- [18] J. Kaipio and E. Somersalo, *Statistical and Computational Inverse Problems*, ser. Applied Mathematical Sciences. Verlag, NY: Springer, 2005, vol. 160.
- [19] T. A. Oliver, G. Terejanu, C. S. Simmons, and R. D. Moser, “Validating predictions of unobserved quantities,” *Computer Methods in Applied Mechanics and Engineering*, vol. 283, pp. 1310–1335, 2015.
- [20] K. Miki, M. Panesi, E. E. Prudencio, , and S. Prudhomme, “Estimation of the nitrogen ionization reaction rate using electric arc shock tube data and bayesian model analysis,” *Physics of Plasmas*, vol. 19, no. 2, 2012.
- [21] K. Miki, M. Panesiand, E. E. Prudencio, and S. Prudhomme, “Probabilistic models and uncertainty quantification for the ionization reaction rate of atomic nitrogen,” *Journal of Computational Physics*, vol. 231, no. 9, pp. 3871–3886, 2012.
- [22] M. Panesi, K. Miki, S. Prudhomme, and A. Brandis, “On the assessment of a bayesian validation methodology for data reduction models relevant to shock tube experiments,” *Computer Methods in Applied Mechanics and Engineering*, vol. 213-216, pp. 383–398, 2012.

- [23] J. Kalyanaraman, Y. Kawajiri, R. P. Lively, and M. J. Realff, “Uncertainty quantification via bayesian inference using sequential monte carlo methods for co₂ adsorption process,” *AICHE Journal*, vol. 62, pp. 3352–3368, 2016.
- [24] T. A. Oliver and R. D. Moser, “Bayesian uncertainty quantification applied to rans turbulence models,” *Journal of Physics: Conference Series*, vol. 318, no. 4, p. 042032, 2011.
- [25] E. B. Albuquerque, D. A. Castello, and L. A. Borges, “Calibration of adhesion models based on bayesian inference,” *Inverse Problems in Science and Engineering*, vol. 24, no. 5, pp. 785–810, 2016.
- [26] G. Wang and S. Chen, “Evaluation of a soil greenhouse gas emission model based on bayesian inference and mcmc: Model uncertainty,” *Ecological Modelling*, vol. 253, pp. 97–106, 2013.
- [27] X. Merle and P. Cinnella, “Bayesian quantification of thermodynamic uncertainties in dense gas flows,” *Reliability Engineering & System Safety*, vol. 134, pp. 305–323, 2015.
- [28] A. Turchi, P. M. Congedo, and T. E. Magin, “Thermochemical ablation modeling forward uncertainty analysis – part i: Numerical methods and effect of model parameters,” *International Journal of Thermal Sciences*, vol. 118, pp. 497–509, 2017.
- [29] M. Mahzari, R. D. Braun, T. R. White, and D. Bose, “Inverse estimation of the mars science laboratory entry aeroheating and heatshield response,” *Journal of Spacecraft and Rockets*, vol. 52, no. 4, pp. 1203–1216, 2015.
- [30] M. Mahzari, “Inverse estimation methodology for the analysis of aeroheating and thermal protection system data,” Ph.D. dissertation, Georgia Institute of Technology, Dec. 2013.
- [31] S. Copeland, M. Mahzari, I. Cozmuta, and J. Alonso, “A statistics-based material property analysis to support ablation simulation uq efforts,” in *3rd AIAA/ASME/ASCE/AHS/ASC Structures, Structural Dynamics and Materials Conference*. Honolulu, HI: AIAA 2012-1763, 2012.
- [32] J. W. Lawson, M. M. Stackpoole, and V. Shklover, “Examination of scanning electron microscope and computed,” NASA Ames Research Center, Moffet Field, CA, Tech. Rep. ARC-E-DAA-TN1167, Oct. 2010.
- [33] J. E. Pavlosky and L. G. S. Leger, “Apollo experience report – thermal protection subsystem,” NASA, Houston, TX, Tech. Rep. TN D-7564, Jan. 1974.
- [34] A. J. Amar, “Modeling of one-dimensional ablation with porous flow using finite control volume procedure,” M.S. thesis, North Carolina State University, 2006.

- [35] R. C. Houtz, ““Orlon” acrylic fiber: Chemistry and properties,” *Textile Research Journal*, vol. 20, no. 11, pp. 786–801, Nov. 1950.
- [36] H. Darcy, *Les fontaines publiques de la ville de Dijon*. Paris, France: Dal-mont, 1856.
- [37] H. Ahn, C. Park, and K. Sawada, “Response of heatshield material at stagnation point of pioneer-venus probes,” *Journal of Thermophysics and Heat Transfer*, vol. 16, no. 3, pp. 432–439, 2002.
- [38] J. Douglas, P. J. Paes-Leme, and T. Giorgi, “Generalized forchheimer flow in porous media,” West Lafayette, IN, Purdue University Technical Report 205, 1993.
- [39] A. Martin and I. D. Boyd, “Non-darcian behavior of pyrolysis gas in a thermal protection system,” *Journal of Thermophysics and heat Transfer*, vol. 24, no. 1, pp. 60–68, 2010.
- [40] H. E. Goldstein, “Kinetics of nylon and phenolic pyrolysis,” Sunnyvale, CA, Lockheed Missiles and Space Company AD667181, 1965.
- [41] E. P. Bartlett, R. M. Kendall, C. B. Moyer, and R. A. Rindal, “An analysis fo the coupled chemically reacting boundary layer and charring ablator, part 1 summary report,” NASA, Washington, D.C., Tech. Rep. CR-1060, June 1968.
- [42] H. Molavi, A. Hakkaki-Fard, I. Pourshaban, M. Fard, and R. Rahmani, “Es-timation of temperature-dependent thermophysical properties of noncharring ablators,” *Journal of Thermophysics and Heat Transfer*, vol. 23, no. 1, pp. 50–58, 2009.
- [43] A. Saltelli, K. Chan, and E. M. Scott, *Sensitivity Analysis*. Wiley, 2000.
- [44] A. Saltelli, *Sensitivity Analysis In Practice*. Wiley, 2004.
- [45] A. Saltelli, *Global Sensitivity Analysis: The Primer*. Chichester, England: Wiley, 2008.
- [46] B. Iooss and P. Lemaître, *Uncertainty Management in Simulation-Optimization of Complex Systems: Algorithms and Applications*. Boston, MA: Springer US, 2015.
- [47] I. M. Sobol, “Global sensitivity indices for nonlinear mathematical models and their monte carlo estimates,” *Mathematics and Computers in Simulation*, vol. 55, no. 1-3, pp. 271–280, 2001.
- [48] R. T. Cox, “Probability, frequency and reasonable expectation,” *American Journal of Physics*, vol. 14, no. 1, pp. 1–13, 1946.

- [49] S. Venturi, “Physics-based stochastic framework for the quantification of uncertainty in non-equilibrium hypersonic flows,” M.S. thesis, Politecnico Di Milano, 2016.
- [50] B. M. Adams, M. S. Ebeida, M. S. Eldred, G. Geraci, J. D. Jakeman, K. A. Maupin, J. A. Monschke, L. P. Swiler, J. A. Stephenss, D. M. Vigil, T. M. Wildey, W. J. Bohnoff, K. R. Dalbey, J. P. Eddy, J. R. Frye, R. W. Hooper, K. T. Hu, P. D. Hough, M. Khalil, and E. M. Ridgway, “Dakota, a multilevel parallel object-oriented framework for design optimization, parameter estimation, uncertainty quantification, and sensitivity analysis: Version 6.6 users manual,” University of California, Davis, CA, Tech. Rep. SAND2014-4633, May 2017.
- [51] S. P. Kenny, L. G. Crespo, and D. P. Diesy, “Uqtools: The uncertainty quantification toolbox – introduction and tutorial,” NASA, Hampton, Virginia, Tech. Rep. NASA/TM-2012-217561, Apr. 2012.
- [52] E. E. Prudencio and K. W. Schulz, “The parallel C++ statistical library QUESO: Quantification of Uncertainty for Estimation, Simulation and Optimization,” in *Euro-Par 2011: Parallel Processing Workshops*. Springer, 2012. [Online]. Available: http://dx.doi.org/10.1007/978-3-642-29737-3_44 pp. 398–407.
- [53] D. P. Kroese, T. Breteton, T. Taimre, and Z. I. Botev, “Why the monte carlo method is so important today,” *Wiley Interdisciplinary Reviews: Computational Statistics*, vol. 6, no. 6, pp. 386–392, 2014.
- [54] A. A. Borovkov, *Probability Theory*. London, UK: Springer London, 2013.
- [55] P. J. Green and A. Mira, “Delayed rejection in reversible jump metropolis-hastings,” *Biometrika*, vol. 88, no. 4, pp. 1035–1053, Dec. 2001.
- [56] A. Mira, “On metropolis-hastings algorithms with delayed rejection,” *Metron*, vol. 59, no. 3-4, pp. 231–241, jan 2001.
- [57] H. Haario, E. Saksman, and J. Tamminen, “An adaptive metropolis algorithm,” *Bernoulli*, vol. 7, no. 2, pp. 223–242, 2001.
- [58] H. Haario, M. Laine, and A. Mira, “Dram: Efficient adaptive mcmc,” *Statistics and Computing*, vol. 16, no. 4, pp. 339–354, 2006.
- [59] A. Gelman and D. B. Rubin, “Inference from iterative simulation using multiple sequences,” *Statistical Science*, vol. 7, no. 4, pp. 457–472, 11 1992.
- [60] E. P. Box and G. C. Tiao, *Bayesian Inference in Statistical Analysis*. New York: Wiley, 1973.

- [61] D. D. Hobson, “Thermocouple lag in transient heat-shield measurements due to thermal mass difference,” *Journal of Heat Transfer*, vol. 118, no. 4, pp. 838–841, 1996.
- [62] W. K. Moen, “Apollo engineering summary. postrecovery report - heat shield instrumentation,” Space Division, North American Rockwell Corporation, CSMS 101 TDR 68-166, 1968.